





## Article

# Optimization of ZnO Nanoparticles' Synthesis via Precipitation Method Applying Taguchi Robust Design

Maria-Anna Gatou <sup>1</sup>, Katerina Kontoliou <sup>2,†</sup>, Eleni Volla <sup>1,†</sup>, Konstantinos Karachalios <sup>2</sup>, Grigorios Raptopoulos <sup>3</sup> , Patrina Paraskevopoulou <sup>3</sup> , Nefeli Lagopati <sup>2,4,\*</sup>  and Evangelia A. Pavlatou <sup>1,\*</sup> 

- <sup>1</sup> Laboratory of General Chemistry, School of Chemical Engineering, National Technical University of Athens, Zografou Campus, 15772 Athens, Greece; mgatou2@mail.ntua.gr (M.-A.G.); elenivolla@gmail.com (E.V.)
- <sup>2</sup> Laboratory of Biology, Department of Basic Medical Sciences, Medical School, National and Kapodistrian University of Athens, 11527 Athens, Greece; kate.kontoliou@gmail.com (K.K.); kwnstantinos98@gmail.com (K.K.)
- <sup>3</sup> Inorganic Chemistry Laboratory, Department of Chemistry, National and Kapodistrian University of Athens, 15771 Athens, Greece; grigorisrap@chem.uoa.gr (G.R.); paraskevopoulou@chem.uoa.gr (P.P.)
- <sup>4</sup> Biomedical Research Foundation, Academy of Athens, 11527 Athens, Greece
- \* Correspondence: nlagopati@med.uoa.gr (N.L.); pavlatou@chemeng.ntua.gr (E.A.P.); Tel.: +30-21074-62362 (N.L.); +30-21077-23110 (E.A.P.)
- † These authors contributed equally to this work.

**Abstract:** Zinc oxide (ZnO) possesses exceptional potential to be utilized in water and wastewater treatment applications, either as a photocatalyst or in membrane incorporation. In the present study, ZnO nanoparticles were synthesized using the precipitation method. The Taguchi approach with the  $L_{32}$  orthogonal array was utilized in order to optimize the experimental conditions for the synthesis of the nanoparticles and to ensure that relatively smaller-sized particles were obtained. The design was characterized by ten factors, where nine of them possessed four levels, while one had two levels. This study's design factors were the type of Zn precursor, the concentration of the Zn precursor, the type of precipitating agent, the precipitation agent's concentration, the type of utilized solvent, the pH value of the solvent, the temperature used during the synthetic procedure, the calcination temperature, the time of stirring during synthesis, as well as the stirring speed. The influences of those factors on the selected response parameters (the average crystallite size, degree of crystallinity, energy band gap ( $E_g$ ), and photodegradation constant ( $k$ )) were then evaluated. XRD analysis and the calculated  $E_g$  values indicated that the hexagonal wurtzite structure was the only crystalline phase present in the produced samples. The photocatalytic efficiency of all ZnO nanoparticles was examined in the degradation of rhodamine B under UV light irradiation. The optimal conditions were achieved using zinc acetate dihydrate as the Zn precursor at a concentration equal to 0.3 M, sodium hydroxide as the precipitating agent (1.5 M), methanol as the solvent (the pH value of the solvent was equal to 13), a temperature during the synthetic procedure of 70 °C, 600 °C as calcination temperature, a 90 min stirring time, and 700 rpm as the stirring speed. The optimized ZnO sample was synthesized based on the aforementioned conditions and thoroughly characterized. The acquired results confirmed the prediction of the Taguchi approach, and the most enhanced  $k$ -value was observed.

**Keywords:** zinc oxide; nanoparticles; Taguchi method; synthesis optimization; precipitation approach; photocatalysis; rhodamine B; organic pollutants; dye degradation



**Citation:** Gatou, M.-A.; Kontoliou, K.; Volla, E.; Karachalios, K.; Raptopoulos, G.; Paraskevopoulou, P.; Lagopati, N.; Pavlatou, E.A. Optimization of ZnO Nanoparticles' Synthesis via Precipitation Method Applying Taguchi Robust Design. *Catalysts* **2023**, *13*, 1367. <https://doi.org/10.3390/catal13101367>

Academic Editors: Giuseppe Mele and Jorge Bedia

Received: 19 August 2023

Revised: 4 October 2023

Accepted: 10 October 2023

Published: 13 October 2023



**Copyright:** © 2023 by the authors. Licensee MDPI, Basel, Switzerland. This article is an open access article distributed under the terms and conditions of the Creative Commons Attribution (CC BY) license (<https://creativecommons.org/licenses/by/4.0/>).

## 1. Introduction

According to the findings presented in the World Water Development Report (2020) [1], the safeguarding of water resources in the context of global climate change has become a pivotal concern in today's prominent worldwide challenges. Currently, natural aquatic ecosystems are vulnerable to an array of hazardous chemical and biological substances

stemming from various origins such as civil society, the public sector, and notably, the industrial sphere.

Multiple sectors, including but not limited to textiles, pharmaceuticals, paper production, printing, cosmetics, as well as food manufacturing, produce a significant volume of wastewater that contains a variety of organic pollutants, including dyes, resulting in contamination. In relation to the textile industry, it is approximated that approximately 200,000 tons of dye are released into aquatic bodies annually during dyeing and finishing processes, primarily due to inefficiencies in the dye application procedure [2]. Even at concentrations lower than 1 mg/L, these dyes contribute color to industrial wastewater, disrupt the penetration of sunlight into water bodies, and disrupt the balance of eutrophication processes [3].

Rhodamine B, which is being widely employed, poses a significant threat to aquatic ecosystems and human health. This particular dye is recognized for its mutagenic, poisonous, chemically inert, and non-biodegradable characteristics, rendering it notably dangerous. It poses a significant potential for causing cancer [4]. The existence of organic dyes, even in minimal quantities, has the potential to result in a range of health issues, such as gastrointestinal problems, irritations, anemia, and other conditions [5]. Hence, it is essential to remove these contaminating dyes from wastewater.

At present, a variety of typical treatment techniques are in use, including methods like chemical precipitation, separation, adsorption, and coagulation [6]. However, these methods often lead to incomplete decomposition of dyes and simply shift the pollutants from one phase to another, resulting in the creation of secondary pollutants that demand further management [7,8]. In the present day, increased attention is directed toward advanced oxidation processes (AOPs), which utilize semiconducting materials as a viable substitute for traditional approaches [9]. The aforementioned procedures offer several benefits, such as reduced equipment demands, indiscriminate oxidation, straightforward operational control, cost efficiency, and complete conversion of organic dyes into harmless byproducts [10]. A unique feature of AOPs is the generation of reactive agents like  $\bullet\text{OH}$ , which facilitate the swift and non-selective oxidation of organic contaminants. Notably intriguing is heterogeneous photocatalysis, employing oxide-based nanomaterials, which proves effective in eliminating water-soluble organic pollutants from both water and wastewater under light exposure [11].

Broadly, the process of photocatalytic degradation involves the utilization of suspended particles in a water solution, acting as photocatalysts, which are exposed to illumination. The role of the photocatalyst is pivotal in this procedure. These materials are semiconductors characterized by an electronic band structure, demonstrating a distinct division between the highest occupied energy band, referred to as the valence band (VB), and the lowest unoccupied band, designated as the conduction band (CB), as determined by an energy band gap ( $E_g$ ). When photons possessing energies equivalent to or surpassing the semiconductor's band gap are absorbed, electron-hole ( $e^-$ - $h^+$ ) pairs are engendered within the semiconductor particles. As these generated carriers move, there is a separation of charges, leading to the generation of various compounds (e.g.,  $\text{H}_2\text{O}$ ,  $\bullet\text{OH}$ , and  $^1\text{O}_2$ ). It is imperative to acknowledge that electrons and holes are also able to recombine without engaging in chemical reactions. The oxidative agents initiate the organic pollutants' decomposition located on or close to the catalytic surface, ultimately culminating in their comprehensive transformation into harmless substances [12].

Metal oxide semiconductors ( $\text{TiO}_2$ ,  $\text{ZnO}$ , etc.) possess remarkable adsorption capacities and serve as effective catalysts due to their elevated reactivity, heightened photosensitivity, extensive specific surface area, cost-efficiency, lack of toxicity, and enhanced catalytic effectiveness in dye photodegradation [13].

In comparison with titanium dioxide ( $\text{TiO}_2$ ), zinc oxide ( $\text{ZnO}$ ) possesses a notable advantage as it absorbs a greater portion of the UV spectrum owing to its efficient recombination of electron-hole pairs [13].  $\text{ZnO}$  exists in three distinct forms: wurtzite, zinc blend, and rock salt [14]. Among them, the wurtzite structure is the thermodynamically stable

phase under normal conditions. Structurally, wurtzite comprises a hexagonal close-packed arrangement of  $O^{2-}$  anions, with half of the tetrahedral sites occupied by  $Zn^{2+}$  cations. The remaining half of the tetrahedral sites and all octahedral sites remain unoccupied. Undoped ZnO exhibits n-type conductivity, which is commonly attributed to inherent defects such as excess zinc at interstitial positions and oxygen deficiencies [15].

Numerous investigations have been conducted on the photodegradation of rhodamine B using ZnO [5,16–18]. However, directly comparing their photocatalytic performances is challenging, if not impossible, due to the significant variation in parameters employed during the synthesis of ZnO particles, which greatly impacts their effectiveness in dye degradation. For instance, Shidpour et al. [19] conducted a study where they assessed the impacts of various ZnO morphologies, including nanowires, nanorods, spherical particles, and welded nanoparticles, on the degradation of methylene blue dye. Their findings revealed that nanowire-shaped structures displayed the most enhanced degradation efficiency. Similarly, Kumaresan and co-researchers [20] noticed a subtle alteration in ZnO's optical band gap due to particle size variations, leading to a 94% degradation rate for rhodamine B dye and demonstrating reliable stability for reuse. Moreover, Xie and his team [21] reported that ZnO structures resembling sheets exhibited superior photocatalytic activity compared with ZnO's spherical structure. Wang et al. [22] synthesized ZnO with morphologies resembling flowers and rods, concluding that ZnO nanoflowers exhibited higher photocatalytic activity compared with ZnO nanorods. In a different study, Sun et al. [23] fabricated ZnO with 3D hierarchical structures consisting of nanosheets and nanoneedles, with the flower-shaped sample displaying an enhanced photocatalytic performance in comparison with the nanosheet and nanoneedle structures. Efforts have been made to enhance the photocatalytic performance of ZnO through adjustments in preparation condition parameters, such as the utilized Zn precursors, the concentration of Zn precursors, as well as the precipitating agents, the pH and temperature during synthesis, the calcination temperature, and the duration of the synthetic reaction. According to existing studies [24], different Zn precursors present slight or no effects on ZnO nanoparticles' crystallite size, yet they substantially alter their structure. In addition, the divergence in ZnO nanoparticles' crystallite sizes depends on the utilized synthetic approaches [25]. The concentration of Zn precursors and the precipitating agents used are factors that possess a vital role in the synthetic route of ZnO nanoparticles, affecting their morphology and crystallite size [26]. More specifically, as the concentration of the zinc salt precursors increases, the crystallite size of the ZnO nanoparticles produced also increases. Similarly, the crystallite size of the zinc oxide nanoparticles also increases as the concentration of the precipitating agents increases [24]. In another study [27], it was observed that increasing the concentration of the Zn precursor salt beyond a certain limit ( $>0.3$  M) led to a decrease in the formation of zinc oxide nanoparticles. Similar observations for the optimization of nanoparticles with different metal ion concentrations have also been reported elsewhere [28]. Furthermore, the pH value of the reaction solution has a fundamental role in ZnO nanoparticles' synthesis [24,27]. Based on conducted studies, ZnO nanoparticles synthesized at lower solution pH values (in acidic conditions), irrespective of the synthetic approach and reaction conditions, are characterized by smaller crystallite sizes compared with those produced in neutral or alkaline conditions. This observation suggests that the acidic environment influences the crystal structure of ZnO, resulting in the formation of smaller crystallites. Conversely, at higher solution pH values, various authors have reported different trends due to the formation of an intermediate compound (zinc hydroxide), which facilitates the development of larger crystallites [24]. In general, varying morphologies of ZnO nanoparticles have been observed at different solution pH levels, with the crystallite size being dependent on the pH of the solution [24]. Temperature proves to be another crucial factor during the synthesis of ZnO nanoparticles [24,27]. In most reported cases, the crystallite size of ZnO nanoparticles tends to grow larger as the synthesis temperature increases. However, it is worth mentioning that there is an exception in a study in which a green synthetic approach for ZnO nanoparticle synthesis was utilized [29].

This exception highlights that variations in the crystallite sizes of ZnO nanoparticles are influenced not only by the reaction temperature but also by the specific synthetic approach employed. Additionally, it has been proven that a direct correlation between the calcination temperature and the size of ZnO nanoparticles persists [24]. It has been observed that regardless of the chosen synthetic approach, solvent, or other conditions utilized during synthesis, increasing the calcination temperature leads to a proportional increase in the crystallite size of the produced ZnO nanoparticles. The calcination temperature also exerts an influence on the morphology of ZnO nanoparticles, with spherical shapes being predominant in the majority of studies' outcomes. The size of ZnO crystallites varies based on the nucleation time, as reported by various researchers [24]. In particular, extended nucleation periods result in the creation of larger crystallite sizes [27]. This may be attributed to particles having an ample amount of time to merge, leading to the generation of larger ZnO particles through subsequent fusion [24].

Previous studies have highlighted the influential roles of reducing particle size and increasing crystallinity in the photocatalytic activity of ZnO. However, these investigations have primarily utilized direct methods, limiting the evaluation of a wide range of parameters. In contrast, statistical methods offer the advantage of optimizing procedures without the need for exhaustive exploration of numerous parameters [30].

Various methods are applied to optimize an experimental procedure. The Taguchi statistical method, as well as data mining and artificial intelligence, are typically chosen in cases of material synthetic processes, saving time and money, and considering the research study from an ethical and ecological point of view [31].

The Taguchi statistical method is widely recognized as a powerful engineering approach used to investigate the chemistry of materials, with a focus on minimizing variation and sensitivity to noise. Taguchi designs maintain a balanced nature, ensuring that each factor is independently analyzed without any factor being given undue weight. In general, the Taguchi method may require a greater number of experiments than other approaches; however, it is more accurate and statistically reliable for the optimization of process parameters. In addition, the use of Minitab software, as in the present study, drastically reduces potentially complicated analysis [32]. Key concepts in Taguchi experimental designs include factors (the variables under study), levels (the assigned values to the factors), the orthogonal array (OA) (a set of arrays used for the experimental design), such as the  $L_{32}$  array (one two-level factor and nine four-level factors) for a specific number of factors and levels, and the optimum conditions falling into three categories: the maximum value as the preferred outcome, the minimum value as the preferred outcome, and a typical value as the optimal choice. Upon completion of the experiments, analysis is conducted based on the OA to achieve various objectives: identifying the optimal conditions to achieve the highest value, assessing the contribution of each factor to the response, and predicting the response under the optimized conditions [33,34].

This study focused on investigating the synthesis of ZnO nanoparticles using the precipitation method. The Taguchi method was employed to optimize the preparation conditions, aiming to achieve a smaller particle size and higher crystallinity, which are known to enhance photocatalytic activity for the degradation of rhodamine B under UV irradiation. The optimized conditions were determined and applied to prepare a sample, which was subsequently examined to assess its characteristics. Moreover, the photocatalytic mechanism involved in the degradation of rhodamine B was investigated using the sample that exhibited the optimum characteristics. The present research is considered a turning point for all researchers who aim to produce pure zinc oxide nanoparticles using the precipitation method, characterized by an exceptionally small crystallite size (3.29 nm) and enhanced photocatalytic properties in the degradation of organic dyes under UV irradiation (100% RhB degradation within 90 min). In addition, the unique feature of this research is the optimization of zinc oxide nanoparticle synthesis, examining quite a large number of parameters involved in the utilized synthetic approach via a facile statistical method.

## 2. Results

### 2.1. Characterization of the Prepared ZnO Samples

#### 2.1.1. XRD Analysis

The indexed peaks in the acquired spectra for all prepared ZnO samples, via the utilization of different synthetic parameters (Tables 1 and 2), are in total alliance with that of bulk ZnO (JCPDS) card no. 36–1451) [35], affirming both their monocrystallinity and hexagonal wurtzite structure [36] (Figure 1a,b).

**Table 1.** Parameters and their relative values for the experimental procedure design.

Synthesis Parameters	Notation	Unit	Levels of Parameters			
			Level 1	Level 2	Level 3	Level 4
Precipitating agent type	PAT	-	NaOH	KOH	-	-
Precursor of Zn	Zn <sub>prec</sub>	-	ZnAc	ZnChlor	ZnNit	ZnSulf
Concentration of Zn precursor	C <sub>Zn</sub>	M	0.1	0.2	0.3	0.4
Concentration of precipitation agent	C <sub>PA</sub>	M	0.5	1.0	1.5	2.0
Solvent type	S <sub>type</sub>	-	DDI-H <sub>2</sub> O	DI-H <sub>2</sub> O	CH <sub>3</sub> OH	CH <sub>3</sub> CH <sub>2</sub> OH
Solvent pH	S <sub>pH</sub>	-	11	12	13	14
Temperature (synthesis)	T <sub>syn</sub>	°C	50	60	70	80
Temperature (calcination)	T <sub>calc</sub>	°C	400	500	600	700
Stirring time	St <sub>t</sub>	min	30	60	90	120
Stirring speed	St <sub>s</sub>	rpm	300	500	700	1000

**Table 2.** Synthesized ZnO samples based on the Taguchi L<sub>32</sub><sub>b</sub> orthogonal array.

Sample ID	PAT	Zn <sub>prec</sub>	C <sub>Zn</sub>	C <sub>PA</sub>	S <sub>type</sub>	S <sub>pH</sub>	T <sub>syn</sub>	T <sub>calc</sub>	St <sub>t</sub>	St <sub>s</sub>
S1	1	1	1 *	1	1	1	1	1	1	1
S2	1	1	2 *	2	2	2	2	2	2	2
S3	1	1	3 *	3	3	3	3	3	3	3
S4	1	1	4 *	4	4	4	4	4	4	4
S5	1	2	1	1	2	2	3	3	4	4
S6	1	2	2	2	1	1	4	4	3	3
S7	1	2	3	3	4	4	1	1	2	2
S8	1	2	4	4	3	3	2	2	1	1
S9	1	3	1	2	3	4	1	2	3	4
S10	1	3	2	1	4	3	2	1	4	3
S11	1	3	3	4	1	2	3	4	1	2
S12	1	3	4	3	2	1	4	3	2	1
S13	1	4	1	2	4	3	3	4	2	1
S14	1	4	2	1	3	4	4	3	1	2
S15	1	4	3	4	2	1	1	2	4	3
S16	1	4	4	3	1	2	2	1	3	4
S17	2	1	1	4	1	4	2	3	2	3
S18	2	1	2	3	2	3	1	4	1	4
S19	2	1	3	2	3	2	4	1	4	1
S20	2	1	4	1	4	1	3	2	3	2
S21	2	2	1	4	2	3	4	1	3	2
S22	2	2	2	3	1	4	3	2	4	1
S23	2	2	3	2	4	1	2	3	1	4
S24	2	2	4	1	3	2	1	4	2	3
S25	2	3	1	3	3	1	2	4	4	2
S26	2	3	2	4	4	2	1	3	3	1
S27	2	3	3	1	1	3	4	2	2	4
S28	2	3	4	2	2	4	3	1	1	3
S29	2	4	1	3	4	2	4	2	1	3
S30	2	4	2	4	3	1	3	1	2	4
S31	2	4	3	1	2	4	2	4	3	1
S32	2	4	4	1	2	4	2	4	3	1

\* All indicated abbreviations (notations) in Table 2 are explained in Table 1 (synthesis parameters), while the indicated numbers correspond to the levels of the parameters (levels 1–4).



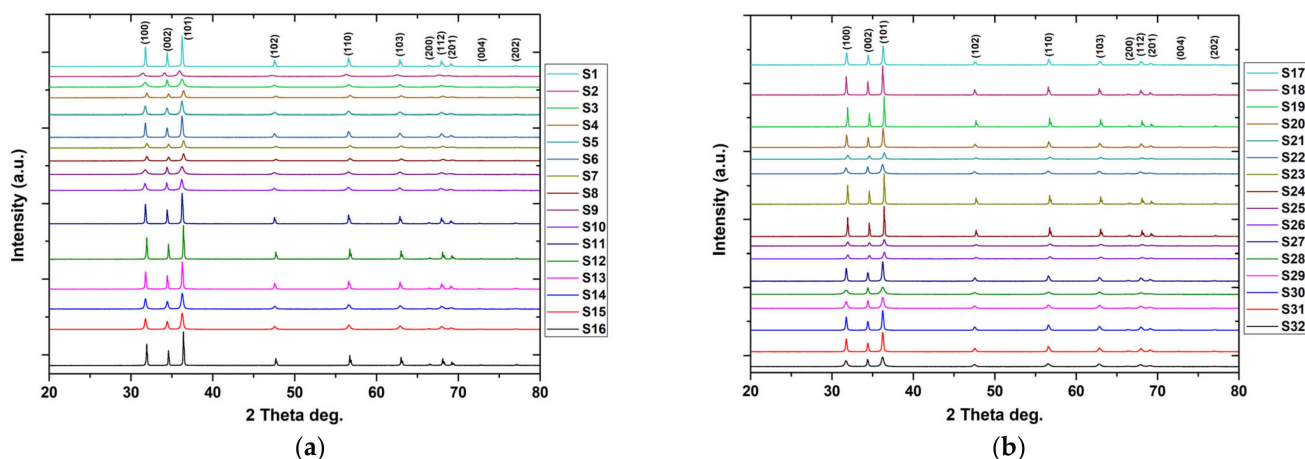


**Figure 1.** XRD diffractograms of the synthesized (a) S1-S16 and (b) S17-S32 ZnO samples.

No other peak corresponding to impurities was observed in the spectra, within the detection limit of the XRD, verifying the pure ZnO nature of the prepared samples [37,38]. The formed peaks at two-theta values,  $31.75^\circ$ ,  $34.41^\circ$ ,  $36.27^\circ$ ,  $47.57^\circ$ ,  $56.64^\circ$ ,  $62.88^\circ$ ,  $66.44^\circ$ ,  $67.96^\circ$ ,  $69.06^\circ$ ,  $72.68^\circ$  and  $76.87^\circ$ , are attributed to the (100), (002), (101), (102), (110), (103), (200), (112), (201), (202), and (004) (Miller indices) planes, respectively. The dissimilarity between the XRD patterns primarily stems from the varying peak intensities, resulting in differences in both the degree of crystallinity and average crystallite size. The calculated values for these parameters are presented in Table 3. The average crystallite size of the produced ZnO samples was estimated using the Debye–Scherrer equation (Equation (1)):

$$D = \frac{0.89\lambda}{\beta \cos \theta} \quad (1)$$

where  $\lambda$  = the X-ray wavelength ( $\lambda = 1.5406 \text{ \AA}$ ), 0.89 stands for Scherrer's constant,  $\beta$  constitutes the full width at half maximum (FWHM) of the peak that was associated with the (101) plane, and  $\theta$  corresponds to Bragg's angle [39].

**Table 3.** Average crystallite size, FWHM, and crystallinity of the synthesized ZnO samples.

Sample ID	Average Crystallite Size (nm) *	Full Width at Half Maximum (FWHM)	Crystallinity (%)
S1	$12.20 \pm 5.3 \times 10^{-3}$	0.1774	$75.85 \pm 2.3 \times 10^{-3}$
S2	$3.52 \pm 4.4 \times 10^{-3}$	0.5166	$73.57 \pm 2.7 \times 10^{-3}$
S3	$3.29 \pm 4.3 \times 10^{-3}$	0.5618	$79.83 \pm 1.1 \times 10^{-3}$
S4	$5.27 \pm 5.0 \times 10^{-3}$	0.3236	$65.20 \pm 1.8 \times 10^{-3}$
S5	$5.50 \pm 6.3 \times 10^{-3}$	0.3364	$77.87 \pm 1.7 \times 10^{-3}$
S6	$8.07 \pm 6.1 \times 10^{-3}$	0.2282	$76.67 \pm 2.4 \times 10^{-3}$
S7	$5.24 \pm 6.2 \times 10^{-3}$	0.3256	$71.13 \pm 2 \times 10^{-3}$
S8	$4.97 \pm 3.9 \times 10^{-3}$	0.3436	$71.84 \pm 1.5 \times 10^{-3}$
S9	$3.63 \pm 3.1 \times 10^{-3}$	0.5088	$73.67 \pm 1.7 \times 10^{-3}$
S10	$5.08 \pm 4.1 \times 10^{-3}$	0.3680	$73.87 \pm 1.6 \times 10^{-3}$
S11	$10.25 \pm 4.1 \times 10^{-3}$	0.1774	$73.58 \pm 2.2 \times 10^{-3}$
S12	$10.69 \pm 2.9 \times 10^{-3}$	0.1595	$74.48 \pm 3.7 \times 10^{-3}$
S13	$9.50 \pm 3.9 \times 10^{-3}$	0.1899	$76.34 \pm 3.1 \times 10^{-3}$
S14	$5.76 \pm 3.8 \times 10^{-3}$	0.3162	$70.23 \times 10^{-3}$
S15	$5.57 \pm 4.4 \times 10^{-3}$	0.3272	$72.69 \pm 2.7 \times 10^{-3}$

Table 3. Cont.

Sample ID	Average Crystallite Size (nm) *	Full Width at Half Maximum (FWHM)	Crystallinity (%)
S16	$11.56 \pm 7.0 \times 10^{-3}$	0.1475	$70.94 \pm 4.4 \times 10^{-3}$
S17	$8.16 \pm 5.1 \times 10^{-3}$	0.2206	$69.77 \pm 2.8 \times 10^{-3}$
S18	$9.07 \pm 5.4 \times 10^{-3}$	0.2039	$69.01 \pm 2.1 \times 10^{-3}$
S19	$12.32 \pm 4.5 \times 10^{-3}$	0.1385	$71.32 \pm 3.4 \times 10^{-3}$
S20	$8.43 \pm 4.5 \times 10^{-3}$	0.2136	$72.19 \pm 5.7 \times 10^{-3}$
S21	$5.15 \pm 5.2 \times 10^{-3}$	0.3316	$75.55 \pm 2.3 \times 10^{-3}$
S22	$4.59 \pm 4.0 \times 10^{-3}$	0.4052	$76.77 \pm 2.8 \times 10^{-3}$
S23	$13.27 \pm 4.9 \times 10^{-3}$	0.1285	$76.21 \pm 6.4 \times 10^{-3}$
S24	$10.43 \pm 4.3 \times 10^{-3}$	0.1635	$68.64 \pm 5.1 \times 10^{-3}$
S25	$5.64 \pm 5.6 \times 10^{-3}$	0.3026	$69.83 \pm 2.8 \times 10^{-3}$
S26	$5.83 \pm 5.6 \times 10^{-3}$	0.2926	$71.73 \pm 3.4 \times 10^{-3}$
S27	$9.01 \pm 7.1 \times 10^{-3}$	0.2042	$75.49 \times 10^{-3}$
S28	$4.82 \pm 6.1 \times 10^{-3}$	0.3838	$76.02 \pm 1.7 \times 10^{-3}$
S29	$5.07 \pm 6.0 \times 10^{-3}$	0.3622	$76.54 \pm 1.4 \times 10^{-3}$
S30	$8.43 \pm 4.6 \times 10^{-3}$	0.2182	$73.76 \pm 3.7 \times 10^{-3}$
S31	$8.80 \pm 4.4 \times 10^{-3}$	0.2092	$75.65 \pm 3.4 \times 10^{-3}$
S32	$4.82 \pm 5.3 \times 10^{-3}$	0.3862	$74.88 \pm 4.3 \times 10^{-3}$

\* Crystallite size was evaluated in compliance with the peak corresponding to (101) plane.

Moreover, the crystallinity index (CI %) was calculated based on Equation (2) [40]:

$$CI (\%) = \frac{\text{Total area of all crystalline peaks}}{\text{Total area of all crystalline and amorphous peaks}} \quad (2)$$

No significant shifts in the peaks' positions were observed, as supported by the acquired XRD diffractograms of the prepared ZnO samples. Nevertheless, alterations in the peaks' intensities in the different samples can be observed, affecting the FWHM and thus resulting in different crystallite sizes.

Among all the indexed planes, that of (101) indicated the most enhanced relative intensity in the entire XRD pattern, implying anisotropic growth and the preferred orientation of the crystallites, given the fact that epitaxial growth along the C-axis in the (001) direction constitutes a distinctive phenomenon in materials possessing a wurtzite structure [41].

Based on the obtained results, the sample annotated as S3 owned the smallest average crystallite size (3.29 nm) and the highest crystallinity (79.83 %) among the produced ZnO samples.

### 2.1.2. Diffuse Reflectance UV–Vis Spectroscopy Analysis (DRS)

Band gap energy ( $E_g$ ) comprises a critical parameter that needs to be taken into consideration in photocatalytic studies. All examined ZnO samples presented absorbance bands, characterized by an absorption edge of <385 nm, which is habitual for the wurtzite crystal phase of ZnO. These bands correspond to the  $O_{2p} \rightarrow Zn_{3d}$  electron transition from the VB to the CB [42]. The DRS measurements of the produced ZnO samples are illustrated in Figure 2a–d.

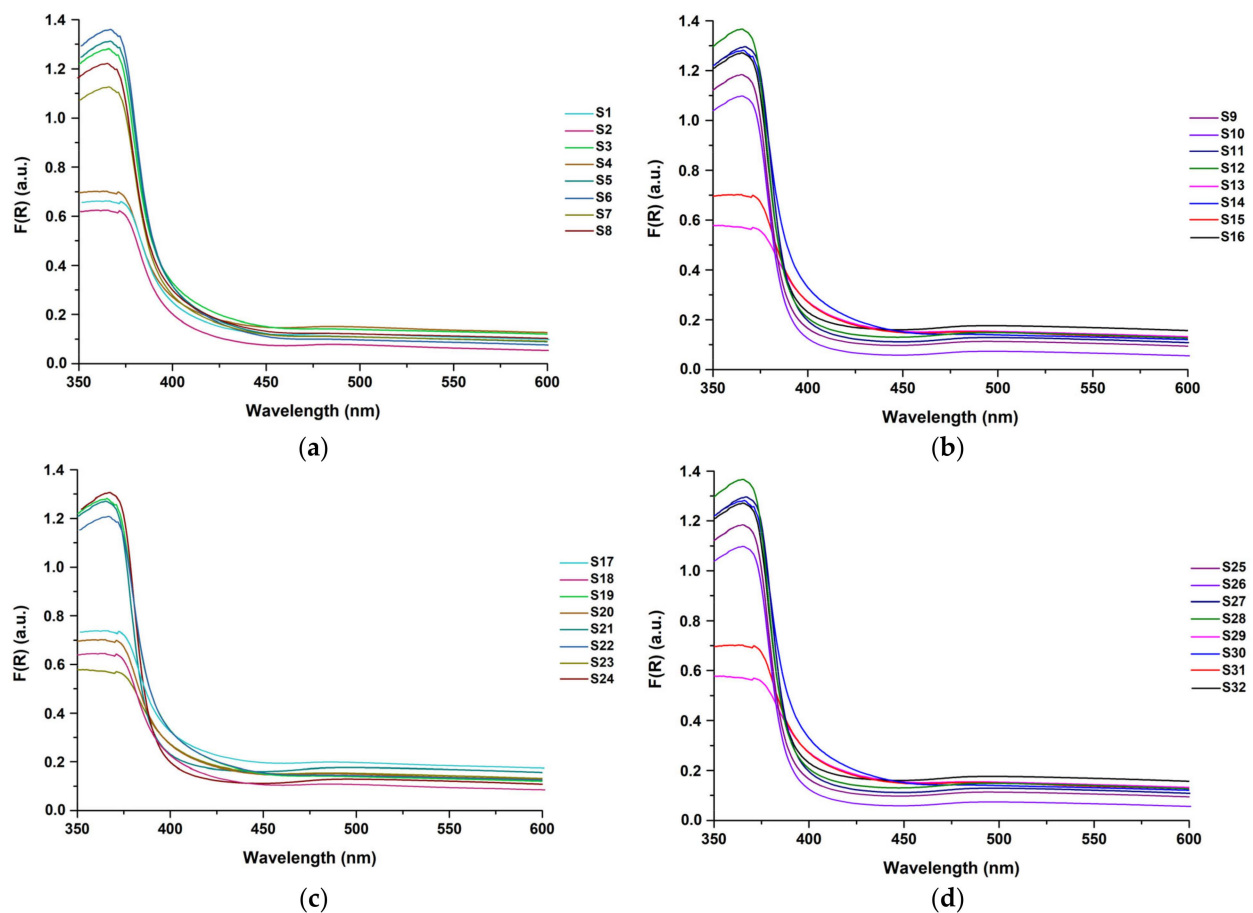


**Figure 2.**  $F(R)$  reflectance as a function of the wavelength for the studied ZnO (a) S1–S8, (b) S9–S16, (c) S17–S24, and (d) S25–S32 samples.

To assess the reflectance of the prepared ZnO samples, the Kubelka–Munk (K–M) method was employed, as shown in Figure 2a–d, using Equation (3) [43]:

$$F(R) = \frac{(1 - R)^2}{2R} \quad (3)$$

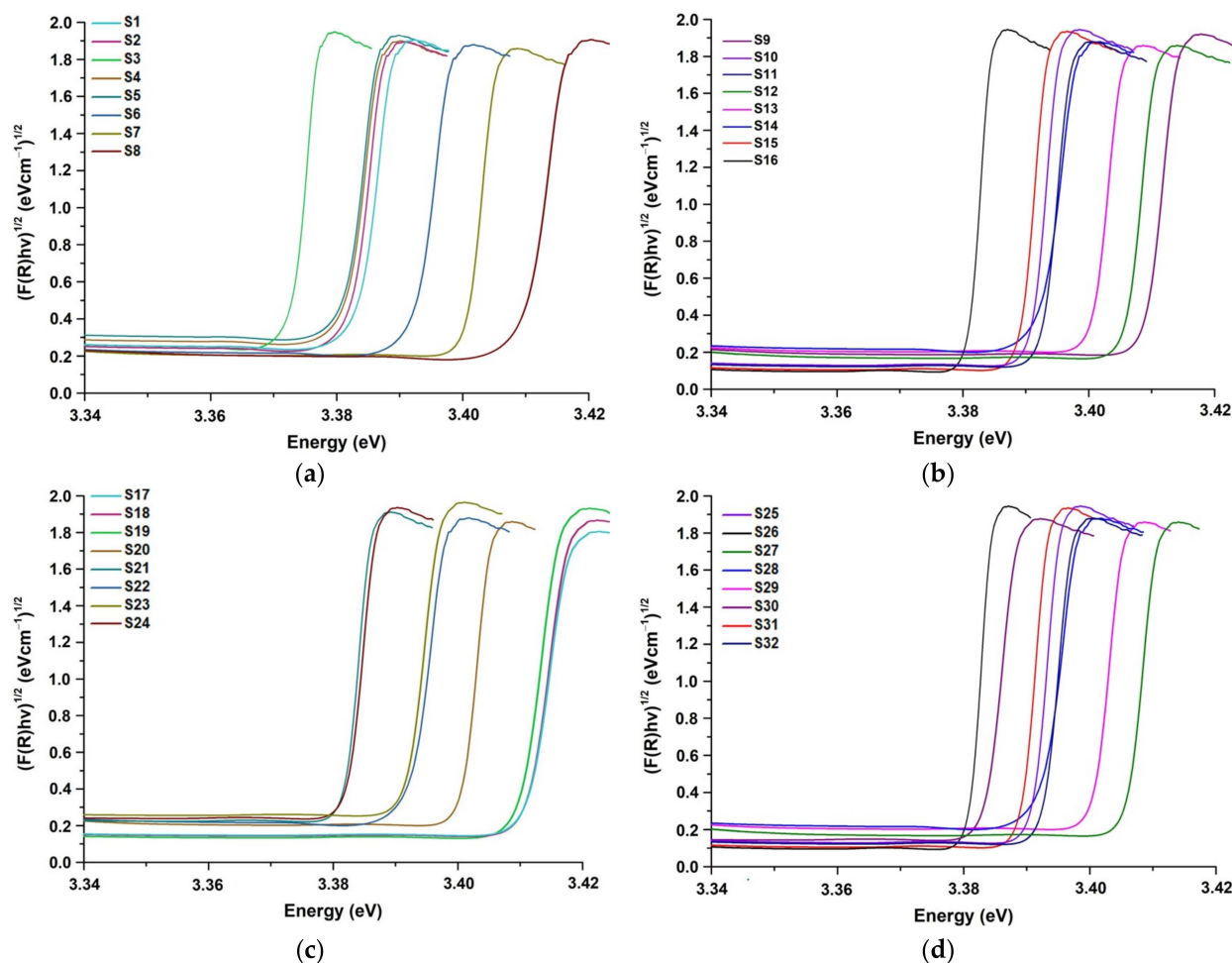
where  $R$  is the reflectance.

Figure 3a–d illustrates the direct energy band gaps of the synthesized ZnO samples using the K–M model vs. energy via the extrapolation of the  $(F(R)h\nu)^{1/2}$  vs.  $h\nu$  spectra's linear region. The energy band gap ( $E_g$ ) was estimated using Tauc's equation (Equation (4)):

$$ah\nu = A(h\nu - E_g)^n \quad (4)$$

where  $E_g$  represents the energy band gap,  $h$  stands for Planck's constant,  $\nu$  corresponds to the frequency,  $\alpha$  is the absorption's coefficient, and  $n$  is equal to  $1/2$  [44].





**Figure 3.** Energy band gaps ( $E_g$ ) of the studied ZnO (a) S1–S8, (b) S9–S16, (c) S17–S24, and (d) S25–S32 samples.

The band gaps of the prepared ZnO samples (S1–S32) were calculated to be between 3.37 eV and 3.41 eV (Table 4), respectively. As can be observed, the estimated values present negligible alterations. However, blue shifts from 3.37 eV (S3) of the ZnO nanospheres to 3.40 eV (S12) of the ZnO nanoflakes (see Figure 9) could be possibly attributed to the quantum confinement of the ZnO nanostructures due to the fact that the flakes' mean thickness is comparable to the Bohr radius of ZnO [21]. The S3 sample achieved the lowest  $E_g$  value (3.37 eV) among all studied samples.

**Table 4.** Energy band gap ( $E_g$ ) values of the prepared ZnO samples (S1–S32).

Sample ID	Energy Band Gap ( $E_g$ , eV)	Sample ID	Energy Band Gap ( $E_g$ , eV)
S1	$3.38 \pm 2.1 \times 10^{-3}$	S17	$3.41 \times 10^{-3}$
S2	$3.38 \times 10^{-3}$	S18	$3.41 \times 10^{-3}$
S3	$3.37 \times 10^{-3}$	S19	$3.41 \times 10^{-3}$
S4	$3.38 \pm 1.5 \times 10^{-3}$	S20	$3.40 \times 10^{-3}$
S5	$3.38 \pm 2.3 \times 10^{-3}$	S21	$3.38 \pm 2.7 \times 10^{-3}$
S6	$3.39 \pm 2.7 \times 10^{-3}$	S22	$3.39 \pm 2.4 \times 10^{-3}$
S7	$3.40 \pm 1.2 \times 10^{-3}$	S23	$3.39 \pm 3.1 \times 10^{-3}$
S8	$3.41 \pm 1.7 \times 10^{-3}$	S24	$3.38 \pm 4.3 \times 10^{-3}$
S9	$3.41 \pm 0.9 \times 10^{-3}$	S25	$3.38 \pm 4.1 \times 10^{-3}$

Table 4. Cont.

Sample ID	Energy Band Gap ( $E_g$ , eV)	Sample ID	Energy Band Gap ( $E_g$ , eV)
S10	$3.38 \pm 1.1 \times 10^{-3}$	S26	$3.38 \pm 2.1 \times 10^{-3}$
S11	$3.39 \pm 0.8 \times 10^{-3}$	S27	$3.40 \pm 2.5 \times 10^{-3}$
S12	$3.40 \pm 3.7 \times 10^{-3}$	S28	$3.39 \times 10^{-3}$
S13	$3.40 \pm 2.4 \times 10^{-3}$	S29	$3.40 \times 10^{-3}$
S14	$3.39 \pm 2.3 \times 10^{-3}$	S30	$3.38 \times 10^{-3}$
S15	$3.39 \pm 3.1 \times 10^{-3}$	S31	$3.39 \pm 2.2 \times 10^{-3}$
S16	$3.38 \times 10^{-3}$	S32	$3.39 \times 10^{-3}$

## 2.2. Photocatalytic Activity of the Prepared ZnO Samples

The photocatalytic efficiency of the prepared ZnO samples was evaluated by measuring their efficiency in decomposing rhodamine B in an aqueous solution upon UV light irradiation. The photocatalytic trials were performed at 25 °C and a pH equal to  $6.64 \pm 0.01$ .

Based on the results obtained via the RhB degradation measurements, the acquired data of the kinetic model investigations under UV light exposure are presented in Figure 4a–d, indicating the relationship between the variation in  $-\ln(C/C_0)$  versus time for the examined ZnO powders. The rate of photocatalytic RhB absorption on the surface of the powders was estimated according to the pseudo-first-order kinetics model, which can be described using the following equation (Equation (5)) [42]:

$$-\ln\left(\frac{C}{C_0}\right) = kt \quad (5)$$

where  $C_0$  and  $C$  correspond to the RhB's initial and reaction time concentrations, respectively,  $k$  represents the apparent rate constant of the photocatalytic oxidation, and  $t$  is the time of irradiation. The slope of the linear fitted plot stands for the apparent rate constants of the examined ZnO samples (S1–S32) (Table 5).

**Table 5.** Apparent rate constant ( $k$ ) values of the examined ZnO samples upon UV light photocatalytic trials based on the pseudo-first-order kinetic model study.

Sample ID	Apparent Rate Constant ( $k$ , min <sup>−1</sup> )	R <sup>2</sup>	Sample ID	Apparent Rate Constant ( $k$ , min <sup>−1</sup> )	R <sup>2</sup>
S1	0.057	0.972	S17	0.055	0.970
S2	0.052	0.995	S18	0.061	0.970
S3	0.065	0.989	S19	0.052	0.966
S4	0.054	0.974	S20	0.057	0.971
S5	0.059	0.975	S21	0.051	0.965
S6	0.058	0.969	S22	0.057	0.988
S7	0.060	0.965	S23	0.058	0.974
S8	0.057	0.963	S24	0.057	0.980
S9	0.054	0.974	S25	0.061	0.987
S10	0.063	0.978	S26	0.063	0.993
S11	0.060	0.967	S27	0.056	0.996
S12	0.059	0.957	S28	0.053	0.994
S13	0.051	0.992	S29	0.051	0.992
S14	0.059	0.975	S30	0.054	0.995
S15	0.058	0.991	S31	0.051	0.989
S16	0.063	0.982	S32	0.048	0.972

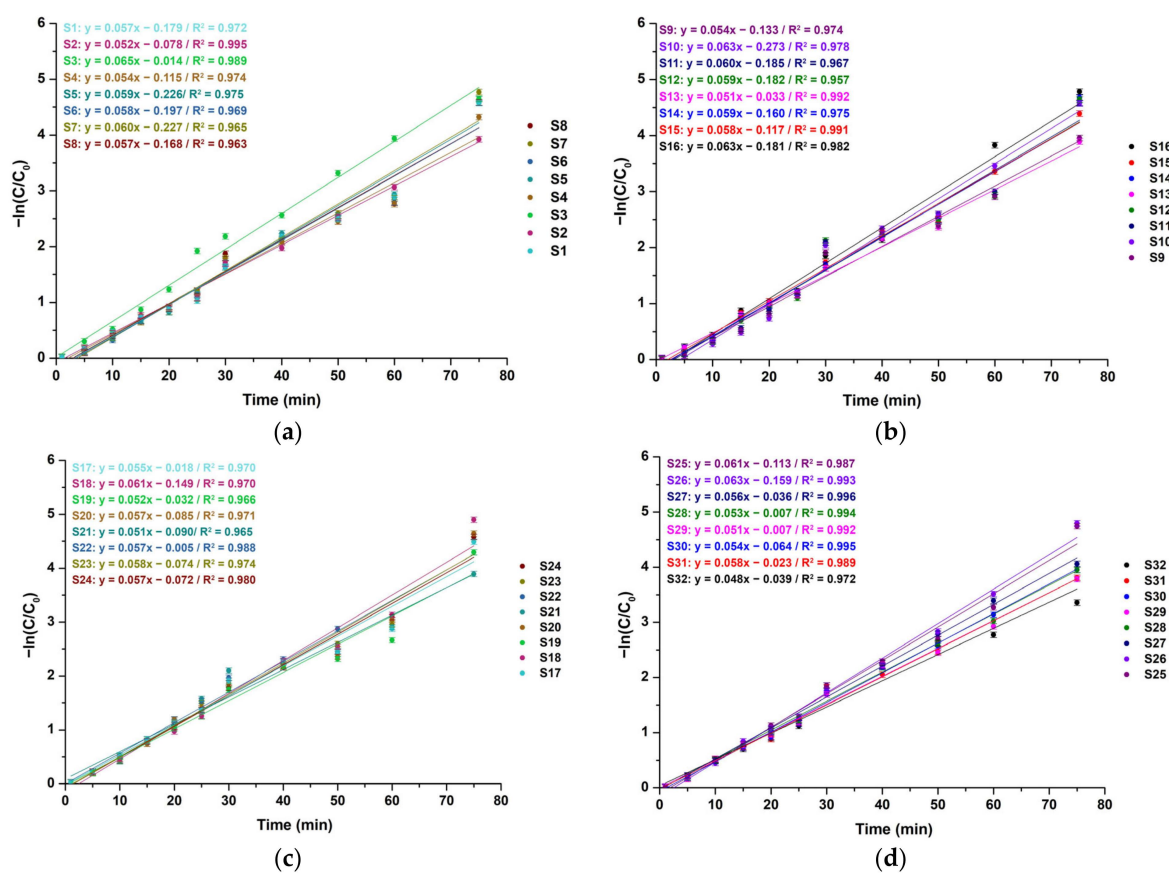


**Figure 4.** Photocatalytic kinetic model studies of the studied ZnO samples, (a) S1–S8, (b) S9–S16, (c) S17–S24, and (d) S25–S32, based on the pseudo-first-order model in UV light photocatalytic experiments.

### 2.3. Results Analysis Based on the Taguchi Approach

Using the provided data in Tables 1 and 2 and following the principles of the Taguchi method, Figures 5–8 are provided to demonstrate the impacts of the specified variables on various outcomes: the average size of the crystallites, the crystallinity, the energy band gap ( $E_g$ ), and the apparent rate constants ( $k$ ) in the degradation of RhB. Additionally, the Minitab software 21.1.0 (Triola Stats, Wappingers Falls, NY, USA) was employed to calculate the percentage of influence and rank the factors with respect to the analyzed parameters, as presented in Table 6.

**Table 6.** Influence percentages and ranks of the factors for the studied parameters.

Factor	$Zn_{prec}$		PAT		$C_{Zn}$		$C_{PA}$		$S_{type}$	
Parameter	%	Rank	%	Rank	%	Rank	%	Rank	%	Rank
D (nm)	12	5	2	9	16	2	14	4	7	7
Crystallinity (%)	15	4	1	10	16	1	16	2	9	6
$E_g$ (eV)	62	1	1	10	4	3	3	7	1	9
$k$ ( $min^{-1}$ )	56	1	6	5	7	3	9	2	1	9
Factor	$S_{pH}$		$T_{syn}$		$T_{calc}$		$St_t$		$St_s$	
Parameter	%	Rank	%	Rank	%	Rank	%	Rank	%	Rank
D (nm)	18	1	1	10	15	3	7	8	8	6
Crystallinity (%)	15	3	4	8	13	5	2	9	9	7
$E_g$ (eV)	3	6	1	8	4	5	7	2	4	4
$k$ ( $min^{-1}$ )	4	8	7	4	4	7	1	10	5	6

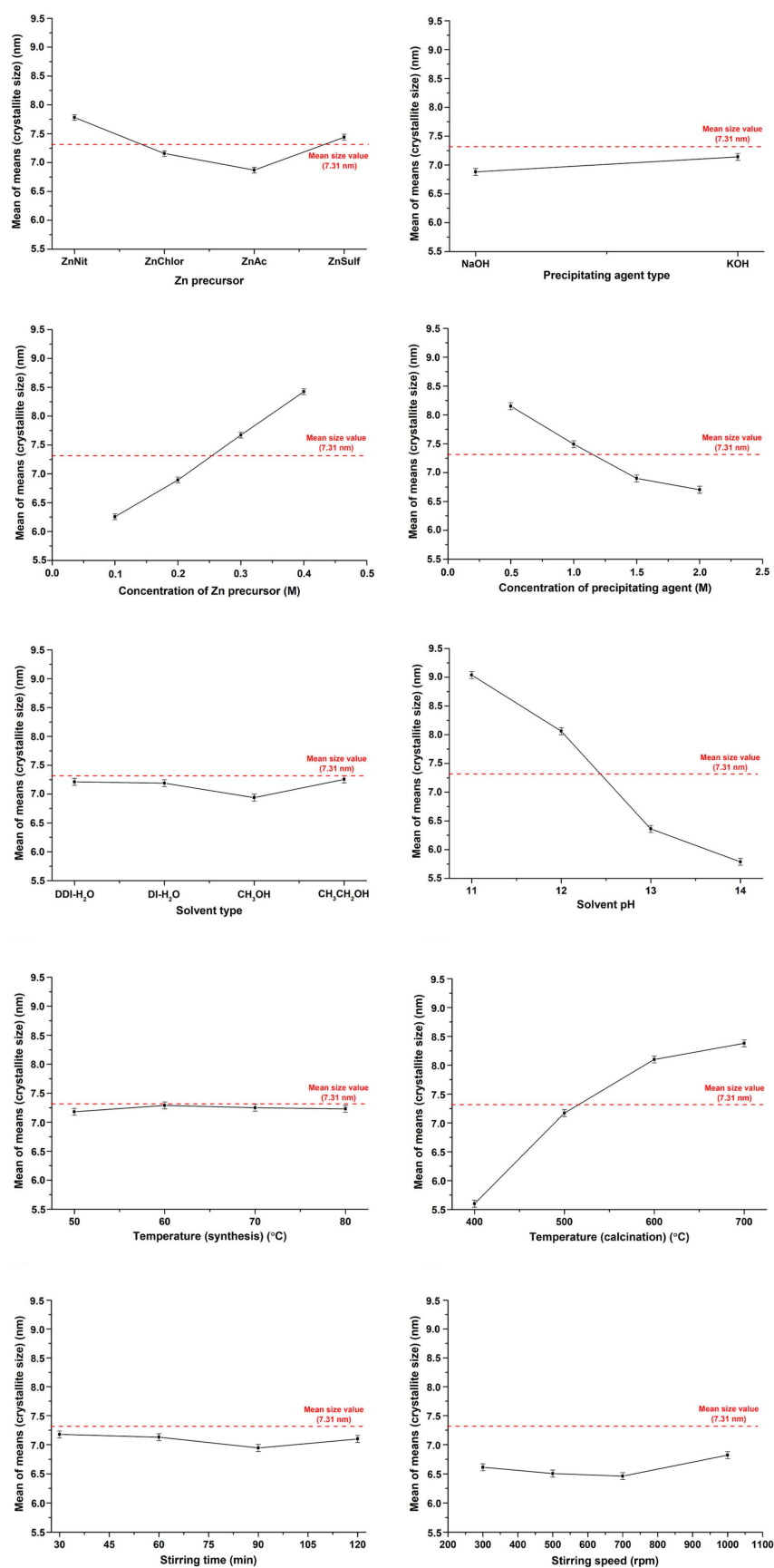


**Figure 5.** Effects of the design parameters on the average crystallite sizes of the prepared ZnO samples.

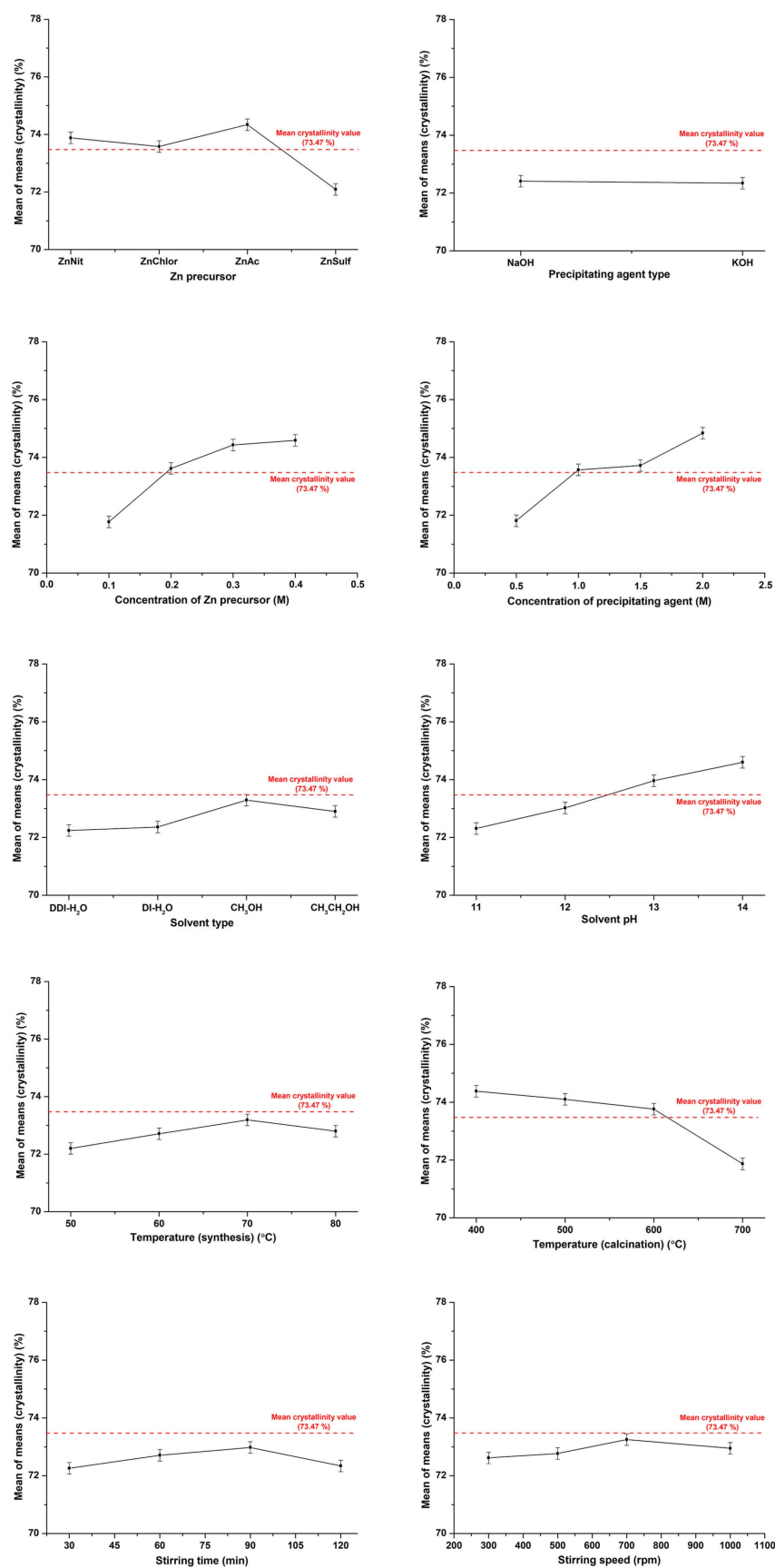
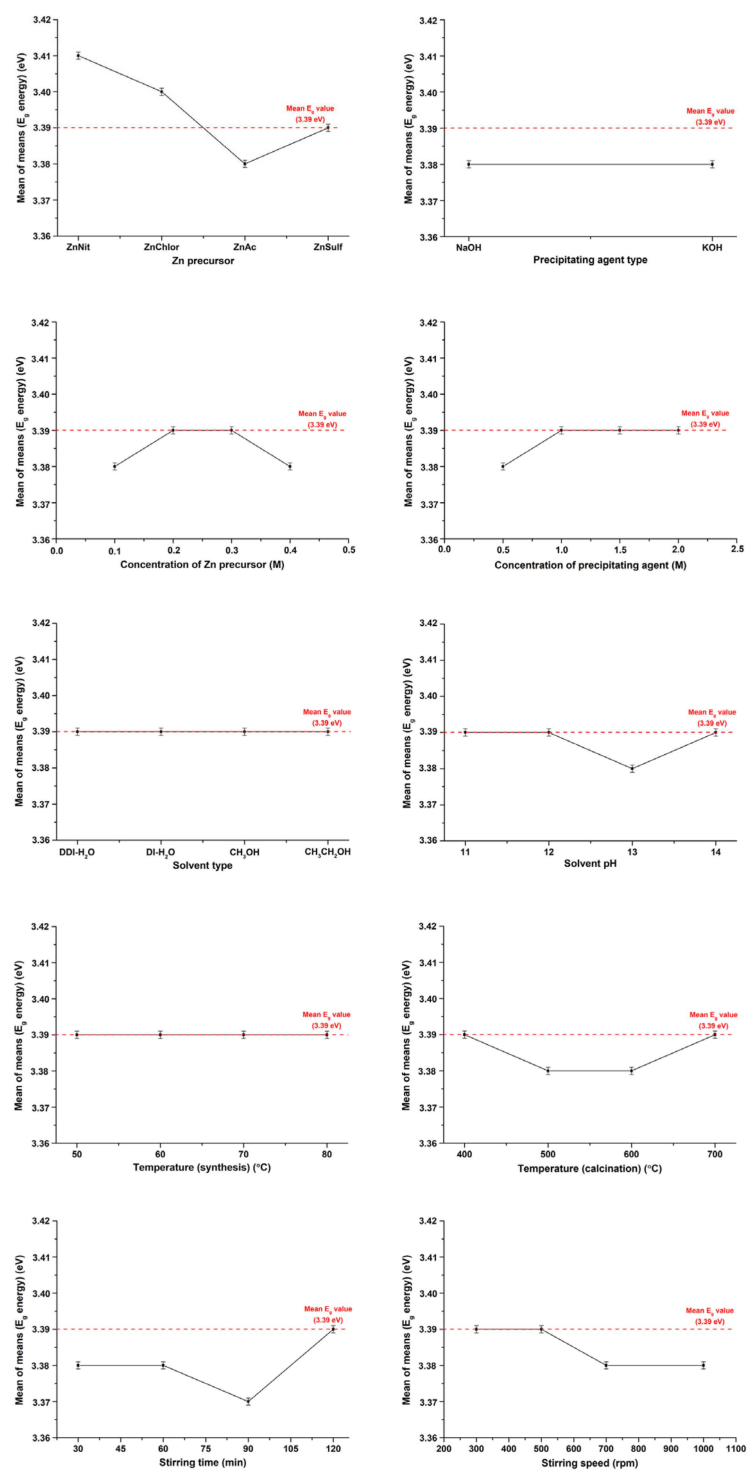
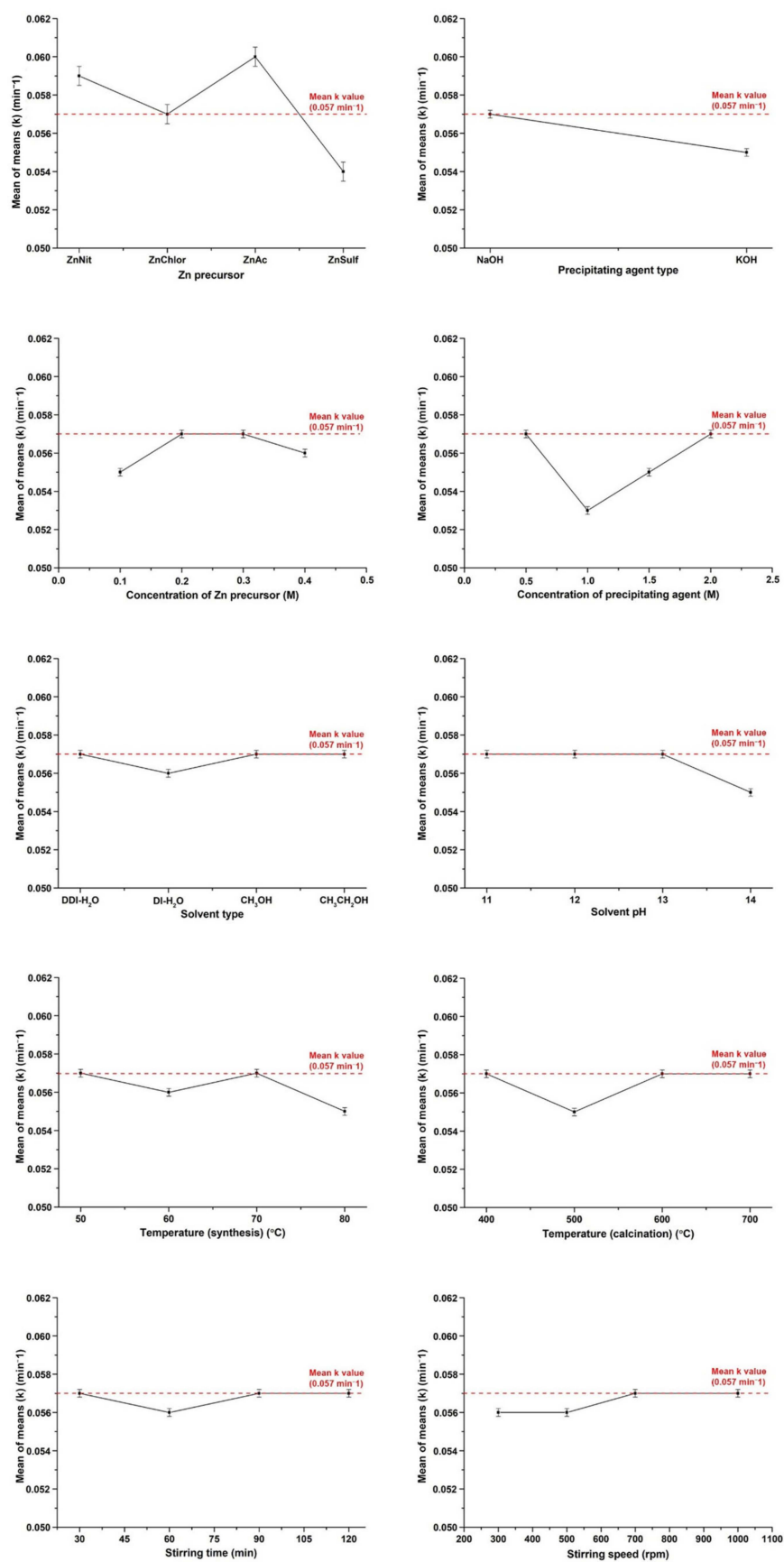


Figure 6. Effects of the design parameters on the crystallinity of the prepared ZnO samples.



**Figure 7.** Effects of the design parameters on the energy band gap ( $E_g$ ) values of the prepared ZnO samples.





**Figure 8.** Effects of the design parameters on the apparent rate constant ( $k$ ) values of the prepared ZnO samples.

### 2.3.1. Average Crystallite Size

The size of crystallites signifies a group of atoms within a crystal that share the same orientation. It represents the dimension of a coherent diffracting domain in the crystalline structure. The formation of point defects and dislocations in the synthesized crystals plays a role in determining their size [45]. Hence, the average crystallite size is a significant variable that impacts both the physical and photocatalytic properties [46]. More specifically, based on existing studies, a small average crystallite size leads to enhanced photocatalytic performance [40].

According to Figure 5, the type and concentration of the Zn precursor, the concentration of the precipitation agent, the pH of the solvent, as well as the calcination temperature, exerted the greatest influence on the average crystallite size. Notably, zinc nitrate and zinc sulfate were responsible for the largest crystallite size, in accordance with our previous research [42]. To validate this observation, FESEM images of four specific samples, namely, sample S3 (containing zinc acetate), sample S5 (containing zinc chloride), sample S12 (containing zinc nitrate), and sample S32 (containing zinc sulfate), were captured and are presented in Figure 9a–d. These images corroborate the findings regarding crystallite size. Samples S3 and S5 exhibit semi-spherical particles with a particle size distribution of 50–100 nm, while samples S12 and S32 exhibit significant changes, with the particles experiencing extensive growth and forming micron-sized hexagonal flakes. The pronounced growth of the particles originating from the zinc nitrate and zinc sulfate precursors contributed to the larger crystallite size observed in this series of samples. Pourrahimi et al. [47] conducted a study on the impact of zinc salts on the grain size of ZnO particles. Based on the obtained results, during ZnO crystallization, the oriented self-assembly and condensation of nanoprisms led to the formation of petals, which were further shaped into octahedrons that interconnected to form polygons. Subsequently, these polygons underwent further growth into larger particles in the case of nitrate and sulfate through the migration and addition of crystallites via dissolution and reprecipitation. Other zinc salts such as chloride and acetate exhibit a stronger ability to prolong the stabilization of the formed crystallites.

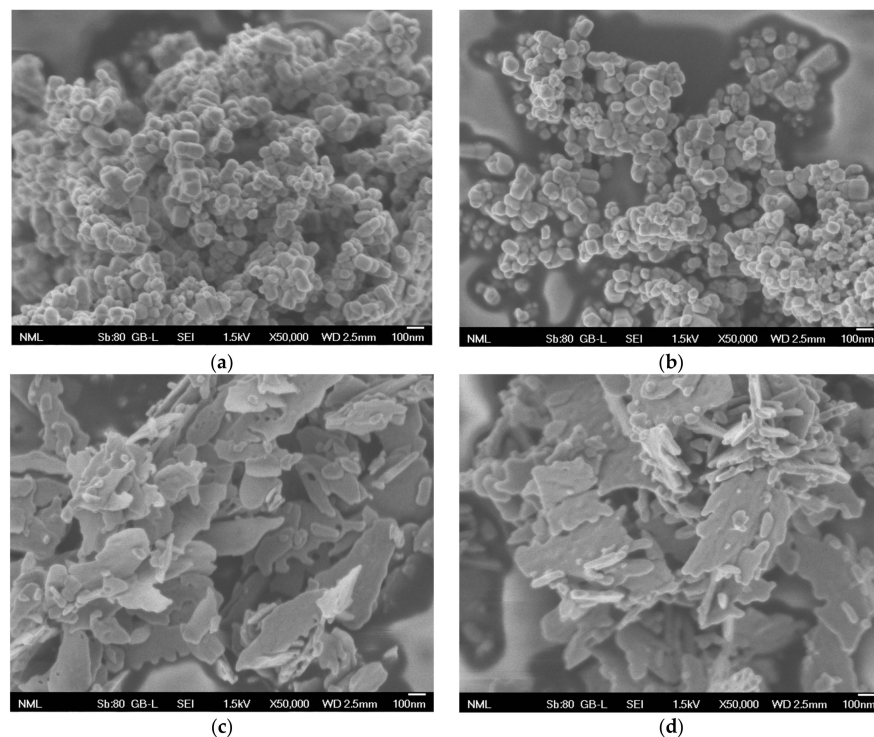


**Figure 9.** FESEM images of the selected ZnO samples: (a) sample S3, (b) sample S5, (c) sample S12, and (d) sample S32 at a  $\times 50,000$  magnification [42].

Additionally, the average crystallite size was found to increase with the increasing concentration of the Zn precursor from 0.1 M to 0.4 M, as proposed in the relevant literature [48], as well as with the increase in the calcination temperature from 400 °C to 700 °C, due to the provision of more energy for nucleation and particle growth [48].

The pH value constitutes another parameter that significantly impacts the average size of the crystallites. Elevating the pH value from 11 to 13 resulted in a decrease in the average crystallite size. At a pH value equal to 11, the solution contained various zinc hydroxide complexes, with  $\text{Zn(OH)}_2$  being the predominant one, leading to the formation of larger particles. When the pH was increased to 13, the condensation process was delayed, resulting in the deceleration of the particles' growth [49].

Finally, it was also observed that the increasing concentration of the examined precipitation agents led to a significant decrease in the average crystallite size, which is in accordance with existing studies' results [50].

### 2.3.2. Crystallinity

Based on the results depicted in Figure 6 and the corresponding analysis, the factors exerting the greatest impact on the degree of crystallinity were (a) the type and concentration of the Zn precursor, (b) the concentration of the utilized precipitating agent, (c) the pH value of the solvent, and (d) the defined temperature during the calcination of the prepared ZnO samples (Table 3).

As for the type of the utilized Zn precursor, the samples that derived from zinc acetate indicated the highest mean crystallinity (74.34%), followed by those prepared with zinc nitrate (73.88%), zinc chloride (73.58%), and zinc sulfate (72.09%), results that are in accordance with a previously conducted study [42]. Additionally, the mean degree of crystallinity presented a gradual enhancement during the elevation of the Zn precursor's concentration, as proposed in the relevant literature [51].

Moreover, the optimal level of crystallinity was attained by adjusting the pH to 14. Increasing the pH value from 11 to 14 resulted in increased crystallinity. This behavior can be attributed to the alteration in the solution component. At higher pH values, ZnO crystallites can form and remain stable [52], which explains the higher crystallinity observed at a pH of 14. Under lower pH conditions, the synthesized ZnO crystallites become unstable, leading to the synthesis of particles with lower crystallinity [53]. The highest pH value facilitates the formation of particles with the highest crystallinity, as it promotes the presence of more  $\text{Zn(OH)}_x$  ions, which serve as the building blocks of the ZnO structure [52].

The observed increase in the calcination temperature promoted the decrease in the crystallinity degree [54].

### 2.3.3. Energy Band Gap ( $E_g$ )

Despite the minor variation in  $E_g$  values, the utilization of zinc acetate in a solution with a pH value equal to 13 and subjected to thermal treatment at 70 °C for 90 min yielded the lowest value. Among the factors considered, the type of Zn precursor exhibited the most significant influence on this particular parameter (Figure 7).

### 2.3.4. Apparent Rate Constant ( $k$ )

The goal of the present study was to produce ZnO nanoparticles via the precipitation method, characterized by enhanced photocatalytic activity under UV light irradiation. Thus, in order to assess the photocatalytic performance of the synthesized ZnO samples, kinetic model studies were conducted, and the photocatalytic capabilities of the samples were represented as  $k$  (Figure 8). The sample that exhibited the highest  $k$  value was obtained by utilizing zinc acetate (0.3 M) as the precursor in a methanol solution, with a pH equal to 13 that was adjusted using sodium hydroxide (1.5 M), followed by stirring at 70 °C and 700 rpm for 90 min, and, finally, calcination at 600 °C (see Table 2).

The choice of zinc acetate as the Zn precursor significantly influenced the size of the crystallites,  $E_g$  values, and ultimately the value of  $k$ . Optimal results, including the

smallest crystallite size, highest crystallinity, and lowest  $E_g$  value, were obtained when this particular precursor was used. These factors collectively contributed to an enhanced photocatalytic behavior, while the highest photoactivity could be achieved when all of them were simultaneously provided. The remaining examined parameters (see Table 1) indicated similar impact rates (see Table 5).

#### 2.4. Synthesis and Characterization of the Optimized ZnO Sample According to the Taguchi Statistical Approach

##### 2.4.1. Synthesis of the Optimized ZnO Sample

Initially, a 0.3 M zinc acetate solution was prepared via the addition of zinc acetate dihydrate to methanol under constant magnetic stirring (700 rpm). The starting pH was equal to  $6.43 \pm 0.01$ . Then, sodium hydroxide (1.5 M) was poured dropwise into the solution until a pH value equal to 13 was obtained. After 90 min at 70 °C, the obtained milky white solution was centrifuged to acquire the white precipitate, which was subsequently triturated and purified via rinsing and centrifugation in order to eliminate potential impurities. The acquired precipitate remained at 100 °C for 1 h to dry and was then calcinated at 600 °C for 3 h, finally leading to the production of a white powder (Figure 10). The reaction that occurred during the synthetic procedure is described using the following chemical reaction (Equation (6)) [42]:

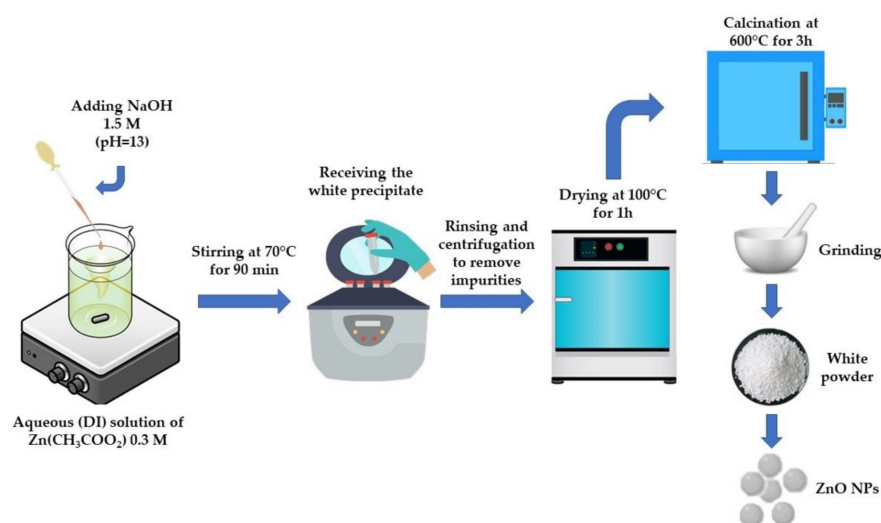
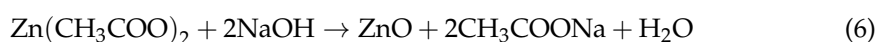


**Figure 10.** Schematic representation of the synthesis of the optimized ZnO sample.

##### 2.4.2. Characterization of the Optimized ZnO Sample

###### XRD Analysis

The annotated peaks in the derived spectrum (Figure 11) are in complete accordance with that of bulk ZnO (JCPDS) card no. 36–1451), as mentioned previously. The absence of impurities was confirmed, as no other peaks were noticed in the spectrum. The high intensity as well as narrowness of the depicted diffraction peaks confirm the highly crystalline structure of the produced ZnO particles [55].

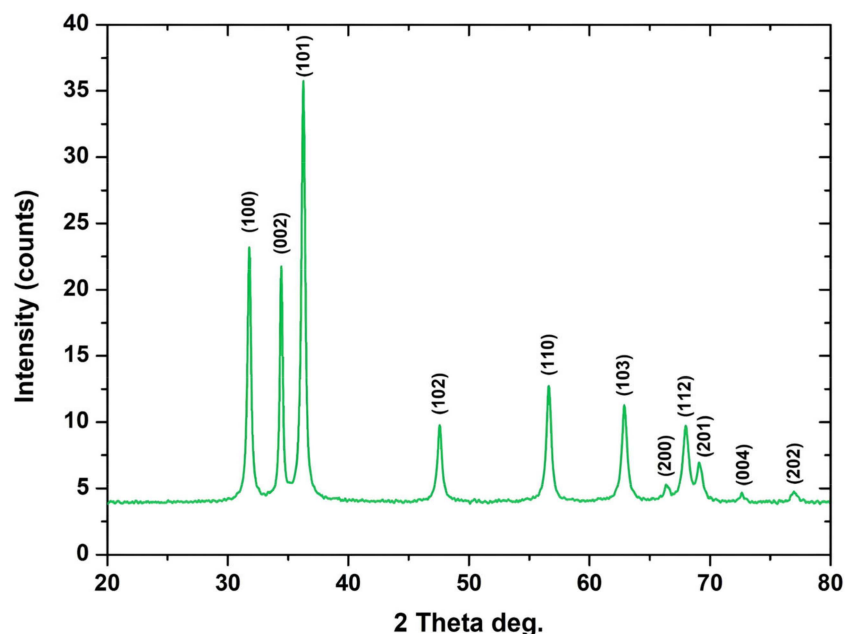


**Figure 11.** XRD diffractogram of the optimized ZnO sample (S3) obtained using the Taguchi statistical approach.

The indexed peaks at  $2\theta = 31.76^\circ, 34.43^\circ, 36.27^\circ, 47.56^\circ, 56.64^\circ, 62.89^\circ, 66.53^\circ, 67.99^\circ, 69.11^\circ, 72.63^\circ$ , and  $76.98^\circ$  are attributed to the (100), (002), (101), (102), (110), (103), (200), (112), (201), (202), and (004) crystal planes, respectively. Calculations for the determination of the crystal lattice indices and interplanar d-spacing were additionally conducted, besides the ascertainment of the crystallinity and average crystallite size that were previously studied. The obtained data are presented in detail in Tables 7 and 8.

**Table 7.** Crystal lattice indices, average crystallite size, FWHM, and crystallinity of the optimized ZnO sample.

Sample	Crystal Lattice Index ( $a = b \neq c$ )			Average Crystallite Size (nm) *	FWHM	Crystallinity (%)
	<i>a</i>	<i>b</i>	<i>c</i>			
S3	2.8152	2.8152	5.2055	$3.290 \pm 7.26 \times 10^{-3}$	0.5618	79.83

\* The crystallite size was estimated based on the (101) plane's peak.

**Table 8.** D-spacing calculations for the optimized ZnO sample.

Bragg's Angle		$d_{hkl}$ (Å)	$d_{hkl}$ (nm)	<i>hkl</i>
$2\theta$	$\theta$			
31.76	15.88	2.8152	0.28152	100
34.43	17.22	2.6027	0.26027	002
36.27	18.14	2.4748	0.24748	101
47.56	23.78	1.9103	0.19103	102
56.64	28.32	1.6238	0.16238	110
62.89	31.45	1.4766	0.14766	103
66.53	33.27	1.4043	0.14043	200
67.99	34.00	1.3777	0.13777	112
69.11	34.56	1.3581	0.13581	201
72.63	36.32	1.3007	0.13007	004
76.98	38.49	1.2377	0.12377	202

The average crystallite size as well as the degree of crystallinity of the optimized ZnO sample were determined utilizing Equations (1) and (2), while the interplanar d-spacing was estimated using Bragg's law equation (Equation (7)), as described below:

$$2d \sin \theta = n\lambda, n = 1 \quad (7)$$

Furthermore, the crystal lattice indices were estimated using Equation (8) [42]:

$$\frac{1}{d_{hkl}^2} = \frac{h^2}{a^2} + \frac{k^2}{b^2} + \frac{l^2}{c^2} \quad (8)$$

#### Micro-Raman Analysis

The Raman spectrum acquired for the optimized ZnO sample is illustrated in Figure 12. The Raman features in the studied ZnO sample correspond to the Raman active modes of the ZnO wurtzite crystal [56].

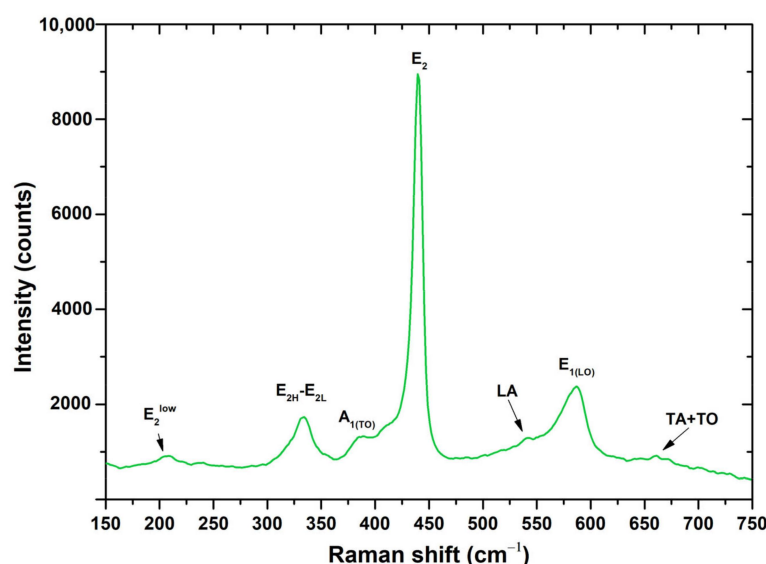


Figure 12. Raman spectrum of the optimized ZnO sample.

The Raman peak presenting the highest intensity in the obtained spectrum is spotted at approximately  $440 \text{ cm}^{-1}$  ( $E_{2H}$  mode), imputed to oxygen vibration [56]. The pronounced lack of symmetry is connected to the disorder in the crystal structure and the interactions between non-harmonic phonons (P-P) [36]. Unlike the  $E_2$  phonons, the polar phonons  $A_1$  and  $E_1$  split into transverse optical (TO) and longitudinal optical (LO) phonons. Consequently, this distinct peak represents a Raman active feature specific to the wurtzite hexagonal phase of ZnO [57].

The second-order mode observed in the low-wavenumber region around  $335 \text{ cm}^{-1}$  is attributed to the difference between  $E_{2H}$  and  $E_{2L}$  [36]. In the middle range of the spectrum for non-activated ZnO, the second-order Raman modes possessing  $A_1$  symmetry ( $484$ ,  $701$ ,  $725$ , and  $742 \text{ cm}^{-1}$ ) are relatively weak and not easily distinguishable, except for the mode observed at  $541 \text{ cm}^{-1}$ . Additionally, acoustical and optical modes integration occur at  $\approx 660 \text{ cm}^{-1}$ .

#### FT-IR Analysis

In the FT-IR spectrum (Figure 13), the presence of ZnO is evident based on the peak detected at  $554 \text{ cm}^{-1}$ . The peak at  $3478 \text{ cm}^{-1}$  corresponds to inter-hydrogen bonding, indicating the presence of water molecules and hydroxyl groups. It was likely influenced by atmospheric humidity during the measurement of the sample [58].



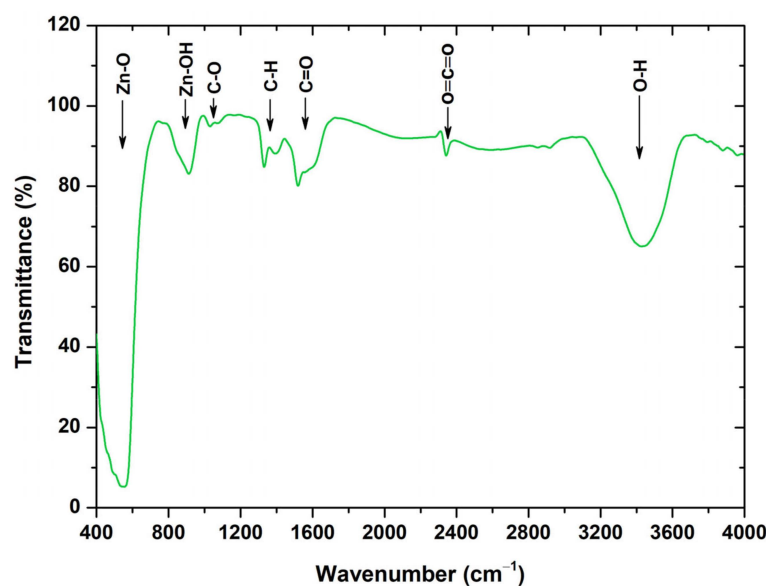


Figure 13. FT-IR spectrum of the optimized ZnO sample.

The peak observed at  $1113\text{ cm}^{-1}$  is associated with the stretching of C-O bonds in primary alcohols. Two additional distinct peaks are particularly noticeable, at  $1520\text{ cm}^{-1}$ , which corresponds to the vibration of a C=O bond and could be indicative of the presence of organic residues that may have persisted after the reaction with acetate, as well as the peak at  $1427\text{ cm}^{-1}$ , possibly corresponding to the bending of carboxylic acid O-H bonds. Furthermore, the identified peak at  $2351\text{ cm}^{-1}$  is attributed to the stretching of carbon dioxide O=C=O bonds [58].

#### N<sub>2</sub>-Sorption Analysis

The N<sub>2</sub>-sorption isotherm for sample S3 is presented in Figure 14.

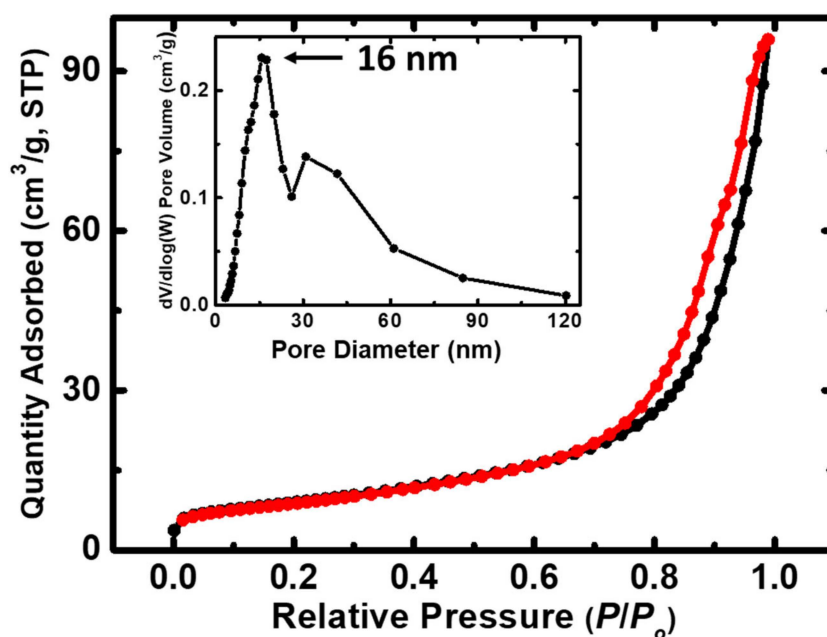


Figure 14. N<sub>2</sub>-sorption diagram of the optimized ZnO sample, as indicated (sorption: black line; desorption: red line). The inset shows the pore size distribution using the BJH method.

It is evident that the synthesized optimized ZnO sample exhibits a type-IV isotherm, with a narrow hysteresis loop and no saturation plateau, which indicates the presence of

mesopores and macropores. The inset in Figure 14 depicts the corresponding pore size distribution, which is determined from the desorption curve using the BJH method. The pore size distribution is quite broad and extends in the mesopore (2–50 nm) as well as in the macropore area (>50 nm), in agreement with the N<sub>2</sub>-sorption isotherm [59–61].

The data of the physical parameters, including the BET surface area, micropore surface area, cumulative volume, and average pore diameter, are compiled in Table 9. The optimized ZnO sample demonstrates an enhanced BET surface area that aligns with the findings of the small crystallite size, as determined from the XRD results (see Table 7).

**Table 9.** Results acquired using the BET method. (a) Specific surface area calculated using Brunauer–Emmett–Teller theory, (b) micropore surface area via t-plot analysis, according to the Harkins and Jura model, (c) cumulative volume of pores between 1.7 and 300 nm from N<sub>2</sub>-sorption data and the BJH desorption method, and (d) average pore diameter, calculated using the  $4V/\sigma$  method. V was set equal to the maximum volume of N<sub>2</sub> adsorbed along the isotherm as  $P/P_0 \rightarrow 1.0$ .

Sample	(a) BET Surface Area (m <sup>2</sup> /g)	(b) Micropore Surface Area (m <sup>2</sup> /g)	(c) Cumulative Volume (1.7–300 nm) (cm <sup>3</sup> /g)	(d) Average Pore Diameter (nm)
S3	32	3	0.1	19

#### Dynamic Light Scattering (DLS) Analysis

The DLS measurements were conducted at a pH value equal to  $6.43 \pm 0.01$ . Figure 15 illustrates the hydrodynamic radius distribution as a function of the scattering light intensity for the synthesized optimized ZnO sample. The sample exhibited a favorable distribution of particle sizes, showing a nearly monodisperse nature (PdI  $\approx 0.1$ ) (Table 10). The size distribution of the particles ranges between 10 and 100 nm, with a peak value of approximately 26 nm. High-purity ZnO nanoparticles, prepared using acetate salt as the precursor and characterized by a mean size of approximately 25 nm, have been previously reported [62], aligning with the experimental findings of the present study. Table 10 presents the obtained data of the DLS measurements.

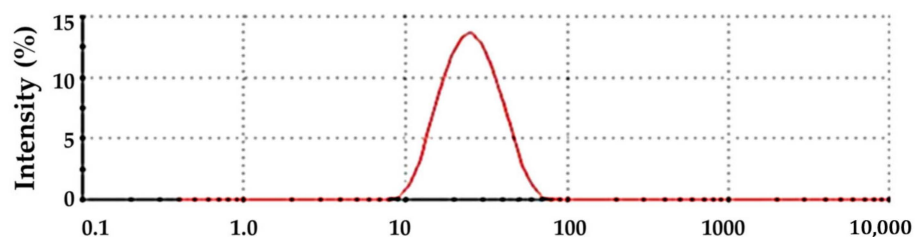


**Figure 15.** Size distribution diagram for the prepared optimized ZnO sample.

**Table 10.** Size distribution results obtained from DLS measurements using an aqueous dispersion solution of the studied ZnO sample.

Sample	Hydrodynamic Diameter ( $D_h$ ) (nm)	PdI *
S3	$27.33 \pm 1.09$	$0.123 \pm 0.011$

\* PdI = polydispersity index.

#### Diffuse Reflectance UV–Vis Spectroscopy Analysis (DRS)

The DRS results for the synthesized sample are depicted in Figure 16a,b. The reflectance of the optimized ZnO sample was evaluated using the Kubelka–Munk (K–M) method, as shown in Figure 16a. Equation (3) was employed for this purpose.

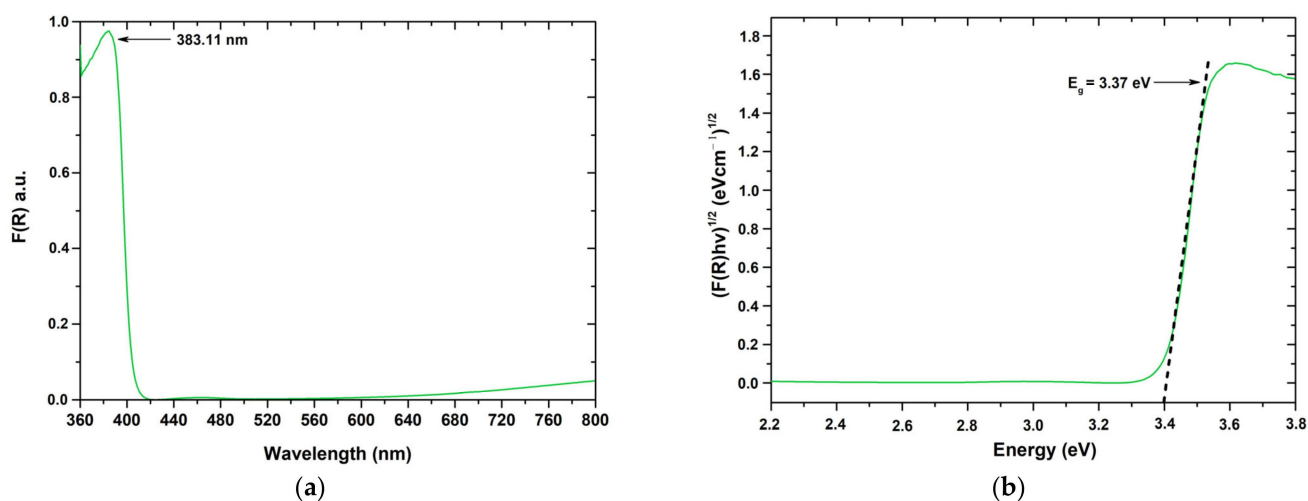


**Figure 16.** (a)  $F(R)$  reflectance as a function of the wavelength for the optimized ZnO sample and (b) energy band gap ( $E_g$ ) of the same sample.

As presented in Figure 16a, the absorption edge is below 385 nm, which is typical for the wurtzite crystal phase of ZnO, as previously mentioned.

Furthermore, Figure 16b demonstrates the direct energy band gap of the produced ZnO sample, utilizing the K-M model vs. energy via the extrapolation of the linear region of the spectrum  $(F(R)h\nu)^{1/2}$  vs.  $h\nu$ .  $E_g$  was evaluated via Tauc's equation (see Equation (4)).

#### FESEM Analysis

The main morphological aspects of the prepared optimized ZnO sample were evaluated via FESEM observation and are depicted in Figure 17a–c.

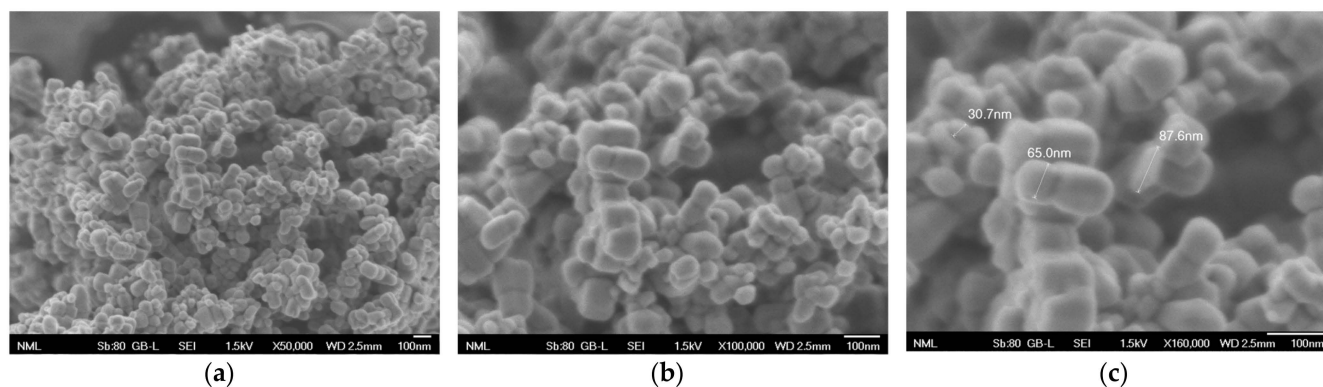


**Figure 17.** Representative FESEM images of the studied optimized sample at (a)  $\times 50,000$ , (b)  $\times 100,000$ , and (c)  $\times 160,000$  magnification.

According to the acquired observation results, the obtained nanoparticles exhibit a combination of spherical and hexagonal shapes. It is widely recognized that zinc oxide (ZnO) can exist in various structures, such as zero-dimensional (0D), one-dimensional (1D), two-dimensional (2D), and three-dimensional (3D) forms. Among these, hexagonal and diamond-shaped structures are the most commonly observed, which aligns with the findings reported in the relevant literature [63].

#### 2.4.3. Photocatalytic Study of the Optimized ZnO Sample

##### Study of the Photocatalytic Efficiency in Degradation of Rhodamine B

The effectiveness of the optimized ZnO sample in photocatalysis was evaluated by measuring the degradation of rhodamine B (RhB) dye in an aqueous solution under UV light

exposure. All photocatalytic experiments were conducted at ambient temperature ( $25\text{ }^{\circ}\text{C}$ ) and a pH value of  $6.43 \pm 0.01$ . Figure 18 illustrates the photocatalytic performance of the investigated sample. Control experiments were also performed to ascertain photolysis (RhB photolysis) and adsorption–desorption equilibrium (RhB dark) without light irradiation (in dark conditions) and under continuous stirring, maintaining the same duration as the photocatalytic process. The observed degradation of rhodamine B under UV light irradiation was found to be  $<1\%$ , indicating that RhB's degradation rate in the absence of the studied photocatalyst is remarkably low. Furthermore, consistent outcomes were acquired from the experiments that took place under dark conditions, confirming the stability of the dye [42].

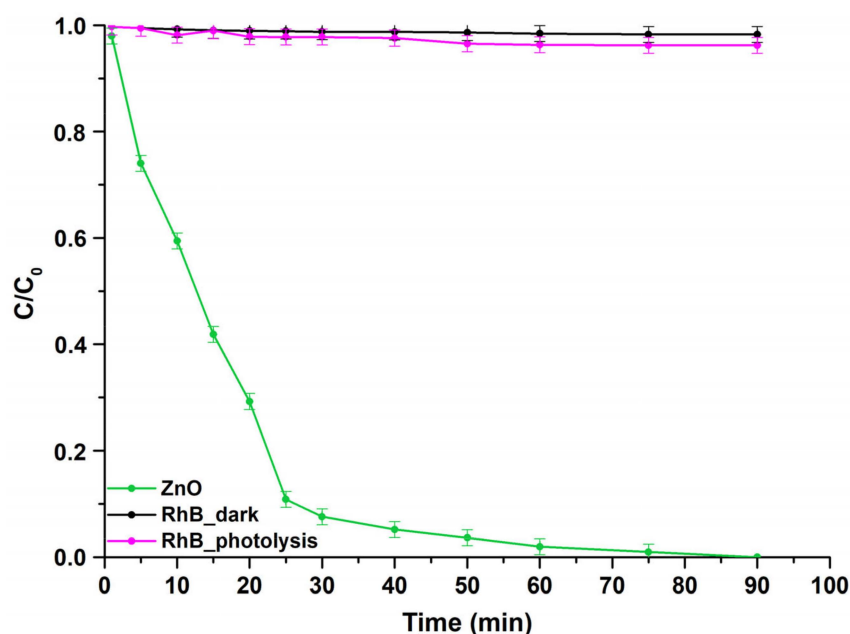


**Figure 18.** Degradation curve of RhB for the optimized ZnO sample vs. time under UV light irradiation. In addition, photolysis and degradation of RhB in the dark are encompassed.

It can be observed that during the photocatalytic trials, the studied optimized sample indicated a high efficiency, attaining total degradation (100%) of the RhB dye within 90 min under UV light irradiation.

Furthermore, Figure 19 displays the UV–visible spectra recorded during the photocatalytic experiments. These spectra were utilized to monitor the degradation rate of RhB over time, investigate its degradation mechanism, as well as assess the photocatalytic efficiency of the sample. Generally, two pathways for RhB degradation are known: (a) N-de-ethylation and (b) disruption of its conjugated structure. When the first degradation mechanism occurs, a blue shift in the maximum absorption is observed, while in the second mechanism, there is no significant blue shift but rather a gradual decrease in absorption over time [64]. In the second proposed degradation pathway, the maximum absorption shifts from 554 nm (which is a characteristic peak of RhB) to 498 nm (blue shift). However, the relevant literature suggests that both pathways contribute simultaneously to the degradation of RhB [65]. The real-time UV–visible spectra obtained for the optimized ZnO sample during the photocatalytic trials under UV light irradiation (Figure 19) evidently demonstrate the presence of both pathways, highlighting their significant roles in the degradation of RhB.

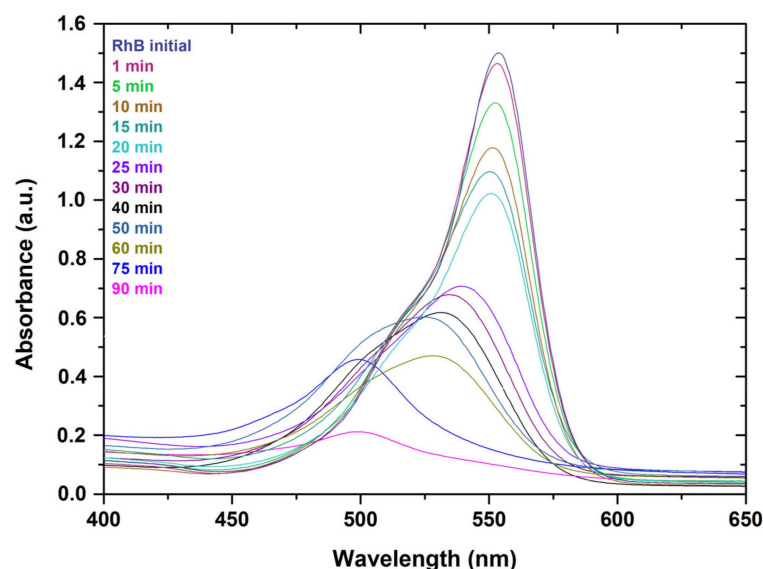


**Figure 19.** Real-time UV–visible spectra obtained under UV light photocatalytic degradation of RhB in the presence of the optimized ZnO sample.

To validate the findings of RhB’s photocatalytic degradation investigations, an additional analysis using TOC was performed in order to assess the percentage of RhB mineralization achieved during the photocatalytic experiments. The mineralization percentage of RhB was calculated using Equation (9):

$$\text{Mineralization (\%)} = \left(1 - \frac{\text{TOC}_{\text{final}}}{\text{TOC}_{\text{initial}}}\right) \times 100 \quad (9)$$

where  $\text{TOC}_{\text{initial}}$  comprises the total organic carbon concentration in the medium before the photocatalytic study, and  $\text{TOC}_{\text{final}}$  stands for the total organic carbon concentration in the medium after the end of photocatalysis [41].

#### Kinetic Model Study

Figure 20a depicts the results obtained from the pseudo-first-order kinetic model study under UV light irradiation, as a variation of  $-\ln(C/C_0)$  vs. time for the mentioned sample that is described using Equation (5). However, the kinetics of photocatalytic trials may also be described using the pseudo-second-order equation (Equation (10)). Compared with the pseudo-first-order kinetics (Figure 20a), the  $R^2$  values of the pseudo-second-order kinetic model study (Figure 20b) are significantly poorer. Table 11 illustrates the kinetic parameters of the studied optimized ZnO sample.

$$\frac{t}{q_t} = \frac{1}{k_2 q_e^2} + \frac{1}{q_e} t \quad (10)$$

where  $q_t$  and  $q_e$  represent the pollutant amount adsorbed at time  $t$  and equilibrium, respectively ( $\text{mg/g}$ ), and  $k_2$  comprises the rate constant ( $\text{g} \cdot \text{mg}^{-1} \cdot \text{min}^{-1}$ ).

**Table 11.** Kinetic parameters of the studied sample under UV light photocatalysis.

Sample	Pseudo-First-Order Kinetic Model		Pseudo-Second-Order Kinetic Model	
	$k_1$ ( $\text{min}^{-1}$ )	$R^2$	$k_2$ ( $\text{g/mg} \cdot \text{min}$ )	$R^2$
S3	0.065	0.989	0.226	0.337

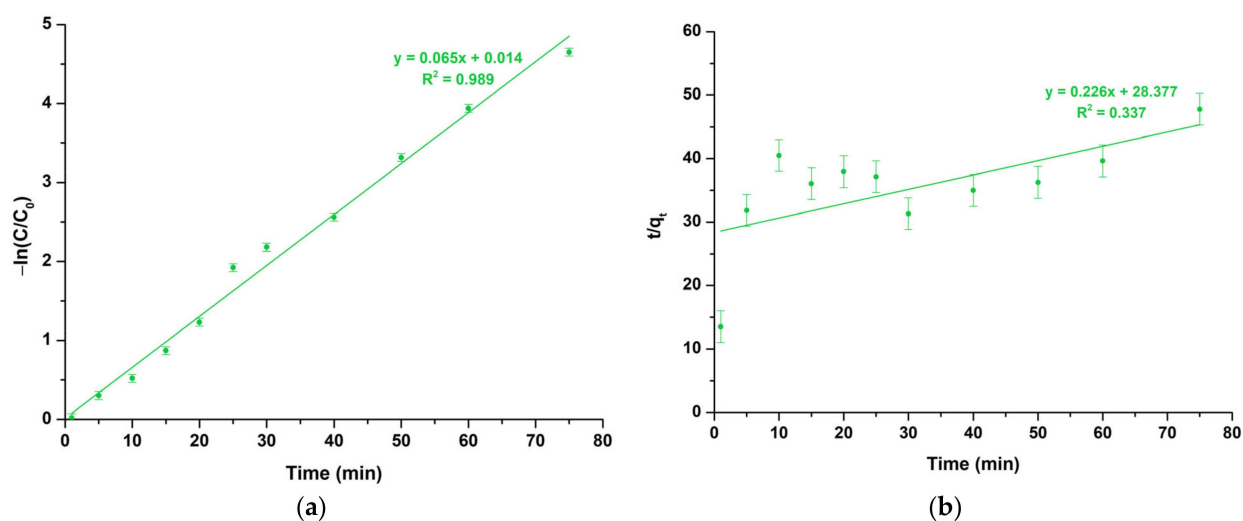
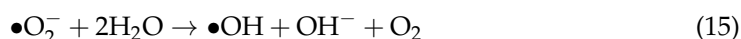
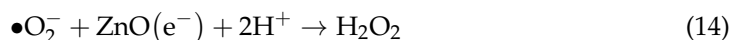
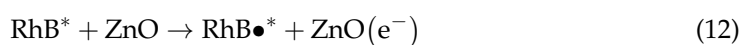


**Figure 20.** Photocatalytic kinetic model studies for the optimized ZnO sample, following (a) the pseudo-first-order model and (b) the pseudo-second-order model, under UV light photocatalytic trials.

#### Mechanism Study

The photocatalytic procedure involving RhB dye can be outlined using the following Equations (11)–(16) [42]:



In the photocatalytic oxidation procedure, various key oxidative species play significant roles, which include superoxide radicals ( $\bullet\text{O}_2^-$ ), electrons ( $e^-$ ), holes ( $h^+$ ), and hydroxyl radicals ( $\bullet\text{OH}$ ). To achieve a deeper understanding of the fundamental mechanism underlying photocatalysis, extensive investigations were conducted to pinpoint the active species. This was accomplished through a series of experiments designed to capture and isolate specific species. Notably, p-benzonquinone (p-BQ), silver nitrate ( $\text{AgNO}_3$ ), disodiummethylenediaminetetraacetate (EDTA-2Na), and t-butanol (t-BuOH) were introduced into the RhB dye solution. These substances were specifically employed to capture and identify superoxide radicals ( $\bullet\text{O}_2^-$ ), electrons ( $e^-$ ), holes ( $h^+$ ), and hydroxyl radicals ( $\bullet\text{OH}$ ), respectively [66].

According to the findings presented in Figure 21, the RhB degradation efficiency of the optimized ZnO sample underwent a significant decrease to  $34.08 \pm 1.25\%$  upon the addition of t-BuOH into the reaction solution. These data provided confirmation that the hydroxyl radicals ( $\bullet\text{OH}$ ) exerted a key influence on RhB's photocatalytic degradation. Additionally, the inclusion of p-BQ,  $\text{AgNO}_3$ , or EDTA-2Na in the photocatalytic reaction solution led to a decrease in RhB's degradation effectiveness from 100% to  $96.34 \pm 1.01\%$ ,  $98.06 \pm 1.13\%$ , and  $95.47 \pm 1.08\%$  respectively, indicating that the superoxide radicals



( $\bullet\text{O}_2^-$ ), photogenerated electrons ( $e^-$ ), and holes ( $h^+$ ) were not the primary reactive species involved in the process.

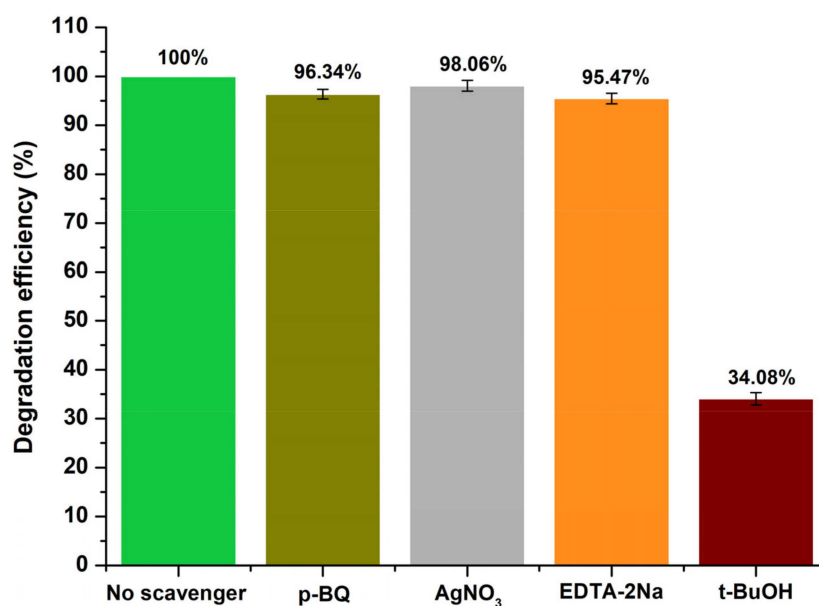


**Figure 21.** Scavenging experiments for the degradation of RhB in the optimized ZnO sample under UV light irradiation.

Based on the scavenging experiment's results, a plausible mechanism is proposed (Figure 22). When exposed to UV light irradiation, ZnO becomes excited, leading to the simultaneous production of  $e^-$  and  $h^+$ . The holes reside in the VB, while the electrons are located in the CB. The electrons in the CB readily take part in reactions with dissolved  $\text{O}_2$  in  $\text{H}_2\text{O}$ , leading to the generation of  $\bullet\text{O}_2^-$ ,  $\text{H}_2\text{O}_2$ , or  $\bullet\text{OH}$  radicals. At the same time, the photoproduced  $h^+$  in the VB is able to directly interact with  $\text{OH}^-$  ions or  $\text{H}_2\text{O}$  molecules bound to the surface, leading to the formation of  $\bullet\text{OH}$  radicals. These highly reactive species, such as  $\bullet\text{OH}$  radicals, relentlessly attack the molecules of rhodamine B until thorough decomposition is achieved, promoting the effective separation of  $e^-$ – $h^+$  pairs and, as a result, enhancing the photocatalytic activity.

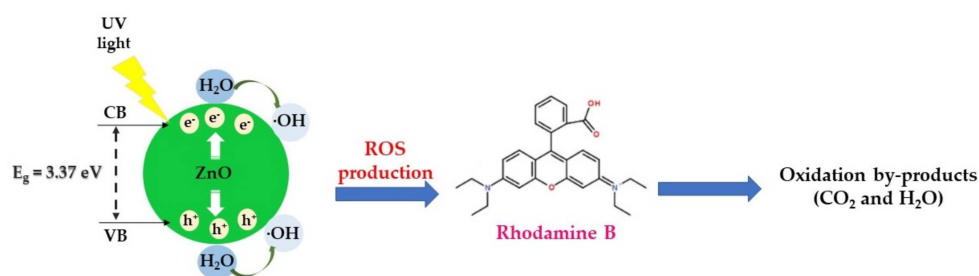


**Figure 22.** The proposed photocatalytic mechanism of the optimized ZnO sample toward degradation of RhB under UV light irradiation.

In the process of photodegrading organic pollutants,  $\bullet\text{OH}$  radicals participate in a redox reaction, transforming long-chain molecules into  $\text{H}_2\text{O}$  and  $\text{CO}_2$  [67]. Nair and colleagues conducted experiments involving both undoped and cobalt-doped ZnO nanoparticles for photocatalysis against a methylene blue (MB) solution. Their findings indicated that pure ZnO demonstrated significantly greater photocatalytic efficiency compared with cobalt-doped ZnO. This enhanced photocatalytic activity can be attributed to the presence of zinc vacancies and interstitial oxygen atoms, creating acceptor states, as well as oxygen vacancies and interstitial zinc atoms, forming donor states [68]. In another study,

Kaur and Singhal synthesized various metal-doped ZnO nanoparticles and assessed their photocatalytic performance against methyl orange (MO). The results revealed that the degradation of MO followed first-order reaction kinetics, with undoped ZnO nanoparticles outperforming their metal-doped counterparts [69]. Furthermore, nanoscale zinc oxide photocatalyst powders were synthesized using the precipitation method, and their photocatalytic effectiveness was evaluated by observing the degradation of MB dye as a test case. The maximum degradation of MB occurred under UV radiation, reaching 81% within 3 h when using photocatalysts prepared via the precipitation method. Assuming a pseudo-first-order reaction kinetics model, this equated to a rate constant of  $8.4 \times 10^{-3} \text{ min}^{-1}$  [4]. In a study by Sultana and colleagues [70], the generation of hydroxyl radicals using zinc oxide (ZnO) synthesized from zinc nitrate ( $\text{Zn}(\text{NO}_3)_2$ ) and sawdust was investigated to degrade MO via photocatalysis. Their experimental setup involved a  $5 \times 10^{-3} \text{ M}$  tannic acid (TA) solution, and they exposed a suspension containing 1 mg of photocatalyst/mL to UVB light (290–320 nm). The results of their research revealed that pure ZnO, without the inclusion of sawdust, exhibited negligible photoactivity and a considerably lower formation of hydroxyl radicals, even when subjected to high-energy UVB irradiation. Conversely, in another investigation [71], ZnO nanowires synthesized via co-precipitation were examined for the degradation of Acid Red 57 dye. This evaluation was conducted using UVA, UVB, and UVC irradiation while varying the calcination temperature. The researchers determined that the optimal degradation performance occurred when calcining at  $400^\circ\text{C}$  and using UVC light (280–100 nm). Moreover, they identified that the primary mechanism responsible for the photodegradation was the generation of hydroxyl radicals.

#### Reusability Study

As depicted in Figure 23, the capability of the optimized ZnO sample to be reused was demonstrated by subjecting it to UV light exposure for five consecutive photocatalytic cycles (catalyst loading = 5 mg;  $\text{pH} = 6.43 \pm 0.01$ ;  $C_{0(\text{RhB})} = 10 \text{ mg/L}$ ). After each cycle of degradation, the sample was treated with centrifugation and multiple rinses with distilled water. Following this, it was dried in a vacuum oven at  $70^\circ\text{C}$  for 24 h in preparation for the subsequent trial, without any additional treatment [72]. Importantly, the ZnO sample synthesized in this manner exhibited remarkable resistance to degradation under UV light, showing a  $\approx 7\%$  reduction ( $6.78 \pm 0.91\%$ ) in its photocatalytic efficiency after undergoing five consecutive cycles. These findings provide proof of the robust stability of the optimized ZnO photocatalyst throughout the repeated cyclic photocatalysis process under UV light irradiation.

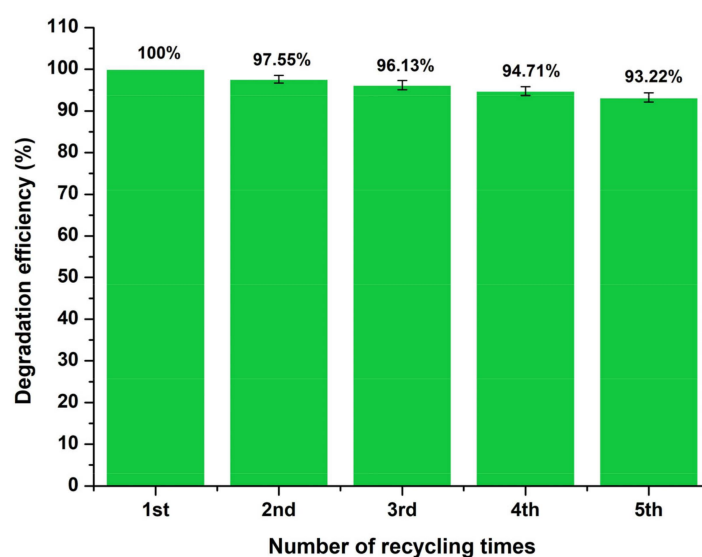


**Figure 23.** Reusability efficiency of the optimized ZnO sample after 5 experimental photocatalytic cycles under UV light irradiation.

### 3. Materials and Methods

#### 3.1. Reagents

Zinc acetate dihydrate ( $\text{Zn}(\text{CH}_3\text{COO})_2 \cdot 2\text{H}_2\text{O}$ , 98%), zinc nitrate hexahydrate ( $\text{Zn}(\text{NO}_3)_2 \cdot 6\text{H}_2\text{O}$ , 98.5%), and rhodamine B (RhB) ( $\text{C}_{28}\text{H}_{31}\text{ClN}_2\text{O}_3$ ,  $M_r = 479.02$  g/mol) were purchased from Penta-Manufacture of Pure and Pharmaceutical Chemicals (Penta-Chemicals Unlimited, Prague, Czech Republic). Zinc chloride ( $\text{ZnCl}_2$ , 98%), methanol ( $\text{CH}_3\text{OH}$ ,  $\geq 99.8\%$ ), and ethanol ( $\text{CH}_3\text{CH}_2\text{OH}$ , 99.8%) were supplied by Fischer Scientific U.K. Limited (Fischer Scientific, Leicester, UK). Zinc sulfate heptahydrate ( $\text{ZnSO}_4 \cdot 7\text{H}_2\text{O}$ , 99.5%) was purchased from ThermoFischer (ThermoFischer GmbH, Kandel, Germany). Sodium hydroxide (NaOH, 99.5%) and potassium hydroxide (KOH, 99%) were purchased from Panreac Quimica SA (Panreac Quimica, Barcelona, Spain). For the photocatalytic mechanism study, p-benzonquinone (p-BQ) ( $\text{C}_6\text{H}_4(=\text{O})_2$ ,  $\geq 98\%$ ; Sigma-Aldrich, Darmstadt, Germany), silver nitrate ( $\text{AgNO}_3$ ,  $>99\%$ ; Sigma-Aldrich, Darmstadt, Germany), disodiummethylenediaminetetraacetate (EDTA-2Na,  $\text{C}_{10}\text{H}_{14}\text{N}_2\text{Na}_2\text{O}_8 \cdot 2\text{H}_2\text{O}$ ,  $\geq 97\%$ ; Sigma-Aldrich, Darmstadt, Germany), and t-butanol (t-BuOH,  $(\text{CH}_3)_3\text{COH}$ ,  $\geq 99.5\%$ ; Sigma-Aldrich, Darmstadt, Germany) were used. Lab-distilled and double-distilled (18.2  $\text{M}\Omega \cdot \text{cm}$ ) water were also used. All reagents and chemicals were pure and used with no further treatment.

#### 3.2. Experimental Procedure Design Based on the Taguchi Approach

The  $L_{32b}$  array of the Taguchi method was utilized to design the experimental plan of the present study. For this reason, ten variable parameters (the precipitating agent type (PAT), precursor of Zn-Zn<sub>prec</sub>, the concentration of Zn precursor ( $C_{\text{Zn}}$ ), concentration of precipitating agent ( $C_{\text{PA}}$ ), solvent type ( $S_{\text{type}}$ ), solvent pH ( $S_{\text{pH}}$ ), temperature during synthesis ( $T_{\text{syn}}$ ), temperature during calcination ( $T_{\text{calc}}$ ), stirring time ( $St_t$ ), and stirring speed ( $St_s$ )) were selected. Nine were adjusted in four levels and one was adjusted in two levels. These variable parameters and their corresponding values are presented in Table 1.

Given the  $L_{32b}$  array of the Taguchi method, the synthesis conditions were specified and are presented in Table 2. The average crystallite size, crystallinity, and band gap energy ( $E_g$ ) were used as intermediate responses, while the photocatalysis degradation rate constant ( $k$ ) was estimated as the response parameter. The optimization of the mentioned parameters was conducted via the comparison of the mean value. The optimized conditions were utilized to synthesize and fully characterize a ZnO sample. Figure 24 describes the main steps of the optimization process using a flowchart.

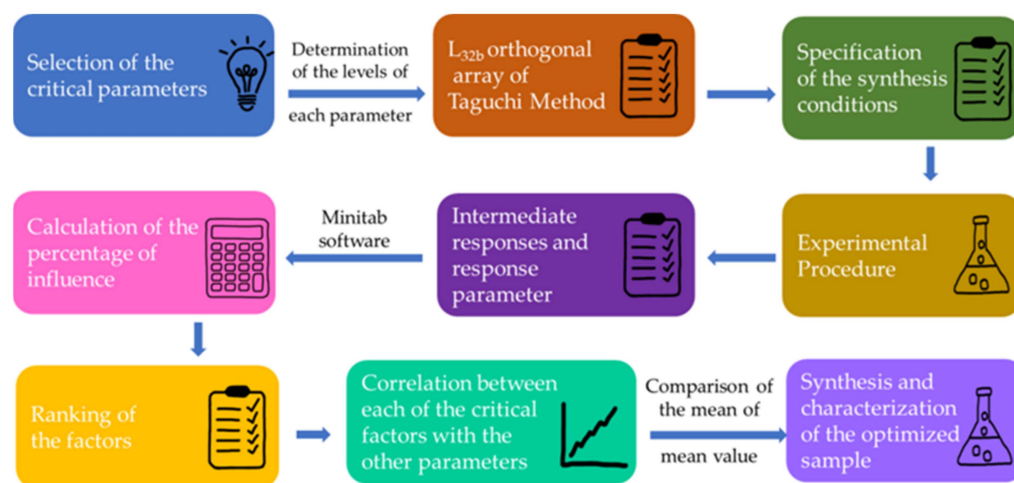


**Figure 24.** Flowchart that describes the main steps of the optimization process.

#### 3.3. Preparation of the ZnO Samples

Thirty-two (32) samples were prepared according to the conditions described in Table 11. Firstly, the Zn precursor and the proper solvent (double-distilled water (DDI-H<sub>2</sub>O),

distilled water (DI-H<sub>2</sub>O), methanol (CH<sub>3</sub>OH), and ethanol (CH<sub>3</sub>CH<sub>2</sub>OH)) were mixed and magnetically stirred at the proper speed, according to Table 2, to gain a uniform solution with a concentration equal to 0.15 M. According to the procedure [42], the appropriate precipitating agent (NaOH or KOH) was added dropwise to the point where the solution reached the relevant pH value. After stirring at the proper time, speed, and temperature, the solution was centrifuged for 10 min at 9000 rpm in order to recover the white precipitate. The precipitate was washed with distilled water and centrifuged thrice in order to remove any organic remains. Each precipitate was left at 100 °C for 1 h to dry, and then, calcination was realized at the appropriate temperature (see Table 2) for 3 h to obtain powder samples. The final products, for convenience purposes, will be called hereinafter S1–S32 (see Table 2).

### 3.4. Characterization of the Prepared ZnO Samples

The X-ray diffractometer that was utilized to study the average crystallite size and crystallinity of the synthesized ZnO samples was a Brucker D8 Advance (Brucker, Berlin, Germany) with CuK $\alpha$  radiation ( $\lambda = 1.5406 \text{ \AA}$ ) at 40 kV and 40 mA. The experimental conditions used were as follows: (a) a 2-theta ( $2\theta$ ) angle ranging from 20 and 80° and (b) a counting diffraction intensity step equal to 0.01°/1.0 s. Additionally, measurements under the same experimental conditions were conducted using a NIST standard LaB<sub>6</sub> powder (Malvern Panalytical Ltd., Malvern, UK) as the reference material in order to calculate the instrumental broadening considered for the Scherrer equation calculations.

The energy band gap ( $E_g$ ) values for all prepared ZnO samples were estimated using an ultraviolet–visible (UV-Vis) spectrometer (Jasco UV/Vis/NIR Model name V-770, Interlab, Athens, Greece) equipped with an integrating sphere (wavelength accuracy =  $\pm 0.3 \text{ nm}$ ), permitting the recording of diffuse reflectance measurements (DRS). For the measurements, the samples were used as received without any further pre-treatment.

Then, the optimized ZnO sample was thoroughly characterized using various techniques. For the XRD and DRS analyses, the same conditions and equipment were used as mentioned above. The morphology of the optimized ZnO sample was analyzed using field-emission SEM (FESEM, JSM-7401F, JEOL, Tokyo, Japan). Observations via field-emission SEM were also conducted to complement the obtained statistical results based on the Taguchi analysis. For the measurements, the samples were used as received without any additional preparation. A beam voltage equal to 1.5 kV was set, while the resolution was equal to 1 nm.

A micro-Raman apparatus (inVia, Renishaw, Wotton-under-Edge, Gloucester, UK) provided with a green laser line ( $\lambda = 532 \text{ nm}$ ) as the excitation source with an average output power of approximately 50 mW was utilized in the present study. Raman spectra were recorded at ambient temperature, and an internal Si reference was used as the calibration of the frequency shift value. For each measured powder, 3 to 10 spots were acquired, and for recording, the following conditions were set: exposure time, 30 s; accumulations equal to 3; power, 1%; spectral range, 100–1000  $\text{cm}^{-1}$ ; and the spectral resolution for all measurements was 2  $\text{cm}^{-1}$ .

In order to complement the micro-Raman results, FTIR spectra were also acquired in the 400–4000  $\text{cm}^{-1}$  range, with a resolution equal to 4  $\text{cm}^{-1}$  at 25 °C with an FTIR JASCO4200 (Oklahoma City, OK, USA) instrument possessing a Ge crystal.

The N<sub>2</sub> adsorption of the synthesized powders was conducted with a ChemBET 3000 Instrument (Yumpu, Diepoldsau, Switzerland) to ascertain the specific surface area BET. Prior to each measurement, the examined samples underwent degassing at 80 °C for 24 h.

Dynamic light scattering (DLS) was used to estimate both the hydrodynamic diameter as well as its distribution for the studied powders' particles that were immersed in distilled water solutions. The incident light was a 633 nm laser, and a 173° scattering angle was arranged for the scattering intensity recording (Malvern Zetasizer Nano ZS, Malvern Panalytical Ltd., Malvern, UK).

RhB's mineralization was estimated by conducting total organic carbon (TOC) analysis (TOC-LCSH/CSN, Shimadzu Scientific Instruments, Columbia, MD, USA) for the exact time points as the ones used during the photocatalytic experiments.

### 3.5. Photocatalytic Activity Study of the Prepared ZnO Samples

The UV light photocatalytic efficiency of the prepared ZnO samples was studied for rhodamine B decomposition, utilizing 0.005 g of each examined sample in a 10 mg·L<sup>-1</sup> rhodamine B (C<sub>28</sub>H<sub>31</sub>ClN<sub>2</sub>O<sub>3</sub>, Penta-Chemicals Unlimited, Prague, Czech Republic) aqueous solution (250 mL) at ambient temperature and a pH equal to 6.64 ± 0.01. Before each photocatalytic experiment (cycles), saturation of the RhB solution for 1 h was carried out through extra pure O<sub>2</sub> (99.999%) flow.

The utilized photoreactor possessed a system of four parallel lamps at a distance of 10 cm above each powder's surface [73]. Blacklight lamps of 368 nm, 830 lumens, and an incident light flux equal to 0.184 μmol quanta/s made by Sylvania (Sylvania, Wilmington, NC, USA) were used as the source of UV light, and all the experiments were carried out under ambient temperature conditions.

The degradation of RhB via photocatalysis was evaluated in the presence of UV light. The absorbance of the ZnO samples prepared in this manner was measured at 554 nm using a Thermo Fisher Scientific Evolution 200 Spectrometer (Thermo Fisher Scientific, Waltham, MA, USA). The C/C<sub>0</sub> ratio, where C represents the concentration of RhB after a specific period of photocatalysis and C<sub>0</sub> is the initial RhB concentration, was determined indirectly by comparing the measured A (absorption at each time) with the initial A (A<sub>initial</sub>) [73].

## 4. Conclusions

The primary objective of this research was to examine the production of ZnO nanoparticles using the precipitation method. To attain a smaller particle size and improved crystallinity, which are recognized as enhancing the photocatalytic effectiveness in degrading rhodamine B under UV irradiation, the Taguchi method was employed to optimize the preparation conditions, more specifically, the Taguchi L<sub>32</sub>b orthogonal array using input variables (Zn precursor, Zn precursor's concentration, precipitating agent type, precipitation agent's concentration, solvent type, solvent pH, synthesis temperature, calcination temperature, stirring time, and stirring speed) and response variables (average crystallite size, crystallinity, energy band gap, and photodegradation constant). Subsequently, the determined optimal conditions were implemented to create a ZnO sample, which was thoroughly characterized utilizing XRD, micro-Raman analysis, FTIR, BET, DLS, DRS, and FESEM to evaluate its properties.

Furthermore, this study delved into investigating the photocatalytic mechanism associated with the degradation of rhodamine B, utilizing the sample that demonstrated the most favorable characteristics. The optimized ZnO sample possessing a hexagonal wurtzite crystalline structure achieved 100% degradation of the RhB dye within 90 min under UV light irradiation, while the pseudo-first-order reaction kinetics provided a realistic description of the photocatalytic degradation of rhodamine B given the calculated R<sup>2</sup> values (0.989).

**Author Contributions:** Conceptualization, M.-A.G., N.L. and E.A.P.; methodology, M.-A.G., K.K. (Katerina Kontoliou), E.V. and K.K. (Konstantinos Karachalios); validation, M.-A.G., K.K. (Katerina Kontoliou), E.V., K.K. (Konstantinos Karachalios), and N.L.; formal analysis, M.-A.G. and N.L., G.R., P.P.; investigation, M.-A.G., K.K. (Katerina Kontoliou), E.V., K.K. (Konstantinos Karachalios), G.R. and N.L.; resources, E.A.P.; writing—original draft preparation, M.-A.G. and E.A.P.; writing—review and editing, M.-A.G., K.K. (Katerina Kontoliou), E.V., K.K. (Konstantinos Karachalios), N.L., G.R., P.P. and E.A.P.; visualization, M.-A.G. and N.L.; supervision, E.A.P. All authors have read and agreed to the published version of the manuscript.

**Funding:** This research received no external funding.

**Data Availability Statement:** Not applicable.



**Acknowledgments:** The authors would also like to acknowledge Evdokia Galata for her assistance with the FESEM measurements conducted at the National Center for Scientific Research “Demokritos”.

**Conflicts of Interest:** The authors declare no conflict of interest.

## References

1. UNESCO. *The United Nations World Water Development Report 2020\_ Water and Climate Change*; UNESCO: Paris, France, 2020.
2. Khan, S.; Malik, A. Toxicity Evaluation of Textile Effluents and Role of Native Soil Bacterium in Biodegradation of a Textile Dye. *Environ. Sci. Pollut. Res.* **2018**, *25*, 4446–4458. [[CrossRef](#)] [[PubMed](#)]
3. Saeed, M.; Khan, I.; Adeel, M.; Akram, N.; Muneer, M. Synthesis of a CoO–ZnO photocatalyst for enhanced visible-light assisted photodegradation of methylene blue. *New J. Chem.* **2022**, *46*, 2224–2231. [[CrossRef](#)]
4. Balcha, A.; Yadav, O.P.; Dey, T. Photocatalytic Degradation of Methylene Blue Dye by Zinc Oxide Nanoparticles Obtained from Precipitation and Sol-Gel Methods. *Environ. Sci. Pollut. Res.* **2016**, *23*, 25485–25493. [[CrossRef](#)] [[PubMed](#)]
5. Dodoo-Arhin, D.; Asiedu, T.; Agyei-Tuffour, B.; Nyankson, E.; Obada, D.; Mwabora, J.M. Photocatalytic Degradation of Rhodamine Dyes Using Zinc Oxide Nanoparticles. *Mater. Today Proc.* **2021**, *38*, 809–815. [[CrossRef](#)]
6. Sansenya, T.; Masri, N.; Chankhanittha, T.; Senasu, T.; Piriyanon, J.; Mukdasai, S.; Nanan, S. Hydrothermal Synthesis of ZnO Photocatalyst for Detoxification of Anionic Azo Dyes and Antibiotic. *J. Phys. Chem. Solids* **2022**, *160*, 110353. [[CrossRef](#)]
7. Vaez, Z.; Javanbakht, V. Synthesis, characterization and photocatalytic activity of ZSM-5/ZnO nanocomposite modified by Ag nanoparticles for methyl orange degradation. *J. Photochem. Photobiol. A* **2020**, *388*, 112064. [[CrossRef](#)]
8. Khataee, A.R.; Pons, M.N.; Zahraa, O. Photocatalytic Degradation of Three Azo Dyes Using Immobilized TiO<sub>2</sub> Nanoparticles on Glass Plates Activated by UV Light Irradiation: Influence of Dye Molecular Structure. *J. Hazard. Mater.* **2009**, *168*, 451–457. [[CrossRef](#)]
9. John Peter, I.; Praveen, E.; Vignesh, G.; Nithiananthi, P. ZnO Nanostructures with Different Morphology for Enhanced Photocatalytic Activity. *Mater. Res. Express* **2017**, *4*, 124003. [[CrossRef](#)]
10. Zhang, D.E.; Ren, L.Z.; Hao, X.Y.; Pan, B.B.; Wang, M.Y.; Ma, J.J.; Li, F.; Li, S.A.; Tong, Z.W. Synthesis and photocatalytic property of multilayered Co<sub>3</sub>O<sub>4</sub>. *Appl. Surf. Sci.* **2015**, *355*, 547–552. [[CrossRef](#)]
11. Ani, I.J.; Akpan, U.G.; Olutoye, M.A.; Hameed, B.H. Photocatalytic Degradation of Pollutants in Petroleum Refinery Wastewater by TiO<sub>2</sub>- and ZnO-Based Photocatalysts: Recent Development. *J. Clean. Prod.* **2018**, *205*, 930–954. [[CrossRef](#)]
12. Sinar Mashuri, S.I.; Ibrahim, M.L.; Kasim, M.F.; Mastuli, M.S.; Rashid, U.; Abdullah, A.H.; Islam, A.; Asikin Mijan, N.; Tan, Y.H.; Mansir, N.; et al. Photocatalysis for Organic Wastewater Treatment: From the Basis to Current Challenges for Society. *Catalysts* **2020**, *10*, 1260. [[CrossRef](#)]
13. Tanji, K.; Navio, J.A.; Chaqroune, A.; Naja, J.; Puga, F.; Hidalgo, M.C.; Kherbeche, A. Fast photodegradation of rhodamine B and caffeine using ZnO-hydroxyapatite composites under UV-light illumination. *Catal. Today* **2022**, *388–389*, 176–186. [[CrossRef](#)]
14. Wu, J.; Xue, D. Progress of Science and Technology of ZnO as Advanced Material. *Sci. Adv. Mater.* **2011**, *3*, 127–149. [[CrossRef](#)]
15. Piras, A.; Olla, C.; Reekmans, G.; Kelchtermans, A.-S.; De Sloovere, D.; Elen, K.; Carbonaro, C.M.; Fusaro, L.; Adriaenssens, P.; Hardy, A.; et al. Photocatalytic Performance of Undoped and Al-Doped ZnO Nanoparticles in the Degradation of Rhodamine B under UV-Visible Light: The Role of Defects and Morphology. *Int. J. Mol. Sci.* **2022**, *23*, 15459. [[CrossRef](#)] [[PubMed](#)]
16. Nandi, P.; Das, D. Photocatalytic Degradation of Rhodamine-B Dye by Stable ZnO Nanostructures with Different Calcination Temperature Induced Defects. *Appl. Surf. Sci.* **2019**, *465*, 546–556. [[CrossRef](#)]
17. Munawar, T.; Yasmeen, S.; Hussain, F.; Mahmood, K.; Hussain, A.; Asghar, M.; Iqbal, F. Synthesis of Novel Heterostructured ZnO–CdO–CuO Nanocomposite: Characterization and Enhanced Sunlight Driven Photocatalytic Activity. *Mater. Chem. Phys.* **2020**, *249*, 122983. [[CrossRef](#)]
18. Neena, D.; Kondamareddy, K.K.; Bin, H.; Lu, D.; Kumar, P.; Dwivedi, R.K.; Pelenovich, V.O.; Zhao, X.-Z.; Gao, W.; Fu, D. Enhanced Visible Light Photodegradation Activity of RhB/MB from Aqueous Solution Using Nanosized Novel Fe–Cd Co-Modified ZnO. *Sci. Rep.* **2018**, *8*, 10691. [[CrossRef](#)]
19. Shidpour, R.; Simchi, A.; Ghanbari, F.; Vossoughi, M. Photo-degradation of organic dye by zinc oxide nanosystems with special defect structure: Effect of the morphology and annealing temperature. *Appl. Catal. A* **2014**, *472*, 198–204. [[CrossRef](#)]
20. Kumaresan, N.; Ramamurthi, K.; Ramesh Babu, R.; Sethuraman, K.; Moorthy Babu, S. Hydrothermally grown ZnO nanoparticles for effective photocatalytic activity. *Appl. Surf. Sci.* **2017**, *418 Pt A*, 138–146. [[CrossRef](#)]
21. Xie, J.; Wang, H.; Duan, M.; Zhang, L. Synthesis and photocatalysis properties of ZnO structures with different morphologies via hydrothermal method. *Appl. Surf. Sci.* **2011**, *257*, 6358–6363. [[CrossRef](#)]
22. Wang, Y.; Li, X.; Wang, N.; Quan, X.; Chen, Y. Controllable synthesis of ZnO nanoflowers and their morphology-dependent photocatalytic activities. *Sep. Purif. Technol.* **2008**, *62*, 727–732. [[CrossRef](#)]
23. Sun, H.; Yu, Y.; Luo, J.; Ahmad, M.; Zhu, J. Morphology-controlled synthesis of ZnO 3D hierarchical structures and their photocatalytic performance. *CrystEngComm* **2012**, *14*, 8626–8632. [[CrossRef](#)]
24. Shaba, E.Y.; Jacob, J.O.; Tijani, J.O.; Suleiman, M.A.T. A critical review of synthesis parameters affecting the properties of zinc oxide nanoparticle and its application in wastewater treatment. *Appl. Water Sci.* **2021**, *11*, 48. [[CrossRef](#)]



25. Rana, N.; Chand, S.; Gathania, A.K. Synthesis and characterization of flower-like ZnO structures and their applications in photocatalytic degradation of Rhodamine B dye. *J. Mater. Sci. Mater. Electron.* **2016**, *27*, 2504–2510. [\[CrossRef\]](#)
26. Phan, C.M.; Nguyen, H.M. Role of capping agent in wet synthesis of nanoparticles. *J. Phys. Chem. A* **2017**, *121*, 3213–3219. [\[CrossRef\]](#)
27. Sandeep, S.; Koteswara Rao, C.; Vijay Rajesh, A.; Sruthi, T.; Surya Prakash, D.V. Studies on characterization and optimization parameters of zinc oxide nanoparticles synthesis. *Int. J. Curr. Res. Rev.* **2022**, *14*, 6–11. [\[CrossRef\]](#)
28. Kumar, S.S.; Venkateswarlu, P.; Rao, V.R.; Rao, G.N. Synthesis, characterization and optical properties of zinc oxide nanoparticles. *Int. Nano Lett.* **2013**, *3*, 30. [\[CrossRef\]](#)
29. Indramahalakshmi, G. Characterization and antibacterial activity of zinc oxide nanoparticles synthesized using *Opuntia ficus indica* fruit aqueous extract. *Asian J. Phys. Chem. Sci.* **2017**, *3*, 1–7. [\[CrossRef\]](#)
30. Khaghanpour, Z.; Naghibi, S. Application of the Taguchi approach to optimize ZnO synthesis via hydrothermally assisted sol-gel method. *Turk. J. Chem.* **2018**, *42*, 20. [\[CrossRef\]](#)
31. Wang, C.-N.; Yang, F.-C.; Nguyen, V.T.T.; Vo, N.T.M. CFD Analysis and Optimum Design for a Centrifugal Pump Using an Effectively Artificial Intelligent Algorithm. *Micromachines* **2022**, *13*, 1208. [\[CrossRef\]](#)
32. Khavekar, R.; Vasudevan, H.; Modi, B. A Comparative analysis of Taguchi methodology and Shainin system DoE in the optimization of injection molding process parameters. *IOP Conf. Ser. Mater. Sci. Eng.* **2017**, *225*, 012183. [\[CrossRef\]](#)
33. Gandhi, P.J.; Murthy, Z.V.P.; Pati, R.K. Optimization of process parameters by Taguchi robust design method for the development of nano-crystals of sirolimus using sonication-based crystallization. *Cryst. Res. Technol.* **2012**, *47*, 53–72. [\[CrossRef\]](#)
34. Singh, M.; Garg, H.K.; Maharana, S.; Yadav, A.; Singh, R.; Maharana, P.; Nguyen, T.V.T.; Yadav, S.; Loganathan, M.K. An experimental investigation on the material removal rate and surface roughness of a hybrid aluminum metal matrix composite ( $\text{Al}_6\text{O}_{61}/\text{SiC}/\text{Gr}$ ). *Metals* **2021**, *11*, 1449. [\[CrossRef\]](#)
35. JCPDS, Powder Diffraction File, Alphabetical Index, Inorganic Compounds; International Centre for Diffraction Data: Newtown Square, PA, USA, 1977.
36. Al-Ariki, S.; Yahya, N.A.A.; Al-A'nsi, S.A.; Jumali, M.H.H.; Jannah, A.N.; Abd-Shukor, R. Synthesis and comparative study on the structural and optical properties of ZnO doped with Ni and Ag nanopowders fabricated by sol-gel technique. *Sci. Rep.* **2021**, *11*, 11948. [\[CrossRef\]](#) [\[PubMed\]](#)
37. Garimella, L.B.V.S.; Dhiman, T.K.; Kumar, R.; Singh, A.K.; Solanki, P.R. One-Step Synthesized ZnO NP-Based Optical Sensors for Detection of Aldicarb via a Photoinduced Electron Transfer Route. *ACS Omega* **2020**, *5*, 2552–2560. [\[CrossRef\]](#)
38. Aljabali, A.A.A.; Obeid, M.A.; Bakshi, H.A.; Alshaer, W.; Ennab, R.M.; Al-Trad, B.; Al Khateeb, W.; Al-Batayneh, K.M.; Al-Kadash, A.; Alsotari, S.; et al. Synthesis, Characterization, and Assessment of Anti-Cancer Potential of ZnO Nanoparticles in an In Vitro Model of Breast Cancer. *Molecules* **2022**, *27*, 1827. [\[CrossRef\]](#)
39. Limón-Rocha, I.; Guzmán-González, C.A.; Anaya-Esparza, L.M.; Romero-Toledo, R.; Rico, J.L.; González-Vargas, O.A.; Pérez-Larios, A. Effect of the Precursor on the Synthesis of ZnO and Its Photocatalytic Activity. *Inorganics* **2022**, *10*, 16. [\[CrossRef\]](#)
40. Supin, K.K.; Parvathy Namboothiri, P.M.; Vasundhara, M. Enhanced photocatalytic activity in ZnO nanoparticles developed using novel *Lepidagathis ananthapuramensis* leaf extract. *RSC Adv.* **2023**, *13*, 1497–1515. [\[CrossRef\]](#)
41. Uribe-López, M.C.; Hidalgo-López, M.C.; López-González, R.; Frías-Márquez, D.M.; Núñez-Nogueira, G.; Hernández-Castillo, D.; Alvarez-Lemus, M.A. Photocatalytic activity of ZnO nanoparticles and the role of the synthesis method on their physical and chemical properties. *J. Photochem. Photobiol. A Chem.* **2021**, *404*, 112866. [\[CrossRef\]](#)
42. Gatou, M.-A.; Lagopati, N.; Vagena, I.-A.; Gazouli, M.; Pavlatou, E.A. ZnO Nanoparticles from Different Precursors and Their Photocatalytic Potential for Biomedical Use. *Nanomaterials* **2023**, *13*, 122. [\[CrossRef\]](#)
43. Cheng, Y.; Luo, F.; Jiang, Y.; Li, F.; Wei, C. The effect of calcination temperature on the structure and activity of  $\text{TiO}_2/\text{SiO}_2$  composite catalysts derived from titanium sulfate and fly ash acid sludge. *Colloids Surf.* **2018**, *554*, 81–85. [\[CrossRef\]](#)
44. Galata, E.; Georgakopoulou, E.A.; Kassalia, M.-E.; Papadopolou-Fermeli, N.; Pavlatou, E.A. Development of Smart Composites Based on Doped- $\text{TiO}_2$  Nanoparticles with Visible Light Anticancer Properties. *Materials* **2019**, *12*, 2589. [\[CrossRef\]](#)
45. Ohira, T.; Yamamoto, O. Correlation between antibacterial activity and crystallite size on ceramics. *Chem. Eng. Sci.* **2012**, *68*, 355–361. [\[CrossRef\]](#)
46. Nandiyanto, A.B.D.; Triawan, F.; Firly, R.; Kishimoto, K. Crystallite Size on Micromechanical Characteristics of  $\text{WO}_3$  Microparticles. *J. Eng. Res.* **2021**, *9*, 268–277. [\[CrossRef\]](#)
47. Pourrahimi, A.M.; Liu, D.; Pallon, L.K.H.; Andersson, R.L.; Martínez Aba, A.; Lagarón, J.-M.; Hedenqvist, M.S.; Ström, V.; Gedde, U.W.; Olsson, R.T. Water-based synthesis and cleaning methods for high purity ZnO nanoparticles—Comparing acetate, chloride, sulphate and nitrate zinc salt precursors. *RSC Adv.* **2014**, *4*, 35568–35577. [\[CrossRef\]](#)
48. Kaningini, A.G.; Azizi, S.; Sintwa, N.; Mokalane, K.; Mohale, K.C.; Mudau, F.N.; Maaza, M. Effect of Optimized Precursor Concentration, Temperature, and Doping on Optical Properties of ZnO Nanoparticles Synthesized via a Green Route Using Bush Tea (*Athrixia phylicoides* DC.) Leaf Extracts. *ACS Omega* **2022**, *7*, 31658–31666. [\[CrossRef\]](#)
49. Alias, S.S.; Ismail, A.B.; Mohamad, A.A. Effect of pH on ZnO nanoparticle properties synthesized by sol-gel centrifugation. *J. Alloys Compd.* **2010**, *499*, 231–237. [\[CrossRef\]](#)
50. Adedokun, O.; Bello, I.T.; Sanusi, Y.K.; Awodugba, A.O. Effect of precipitating agents on the performance of ZnO nanoparticles-based photo-anodes in dye-sensitized solar cells. *Surf. Interfaces* **2020**, *21*, 100656. [\[CrossRef\]](#)

51. Mai, H.H. The influence of precursor concentration on the crystallinity and morphology of ZnO nanorods grown on the printed circuit board substrate. In Proceedings of the 2020 International Conference on Information Technology and Nanotechnology (ITNT), Samara, Russia, 26–29 May 2020; pp. 1–3. [\[CrossRef\]](#)
52. Søndergaard, M.; Bøjesen, E.D.; Christensen, M.; Iversen, B.B. Size and Morphology Dependence of ZnO Nanoparticles Synthesized by a Fast Continuous Flow Hydrothermal Method. *Cryst. Growth Des.* **2011**, *11*, 4027–4033. [\[CrossRef\]](#)
53. McBride, R.A.; Kelly, J.M.; McCormack, D.E. Growth of well-defined ZnO microparticles by hydroxide ion hydrolysis of zinc salts. *J. Mater. Chem.* **2003**, *13*, 1196–1201. [\[CrossRef\]](#)
54. Ismail, A.M.; Menazea, A.A.; Kabary, H.A.; El-Sherbiny, A.E.; Samy, A. The influence of calcination temperature on structural and antimicrobial characteristics of zinc oxide nanoparticles synthesized by sol–gel method. *J. Mol. Struct.* **2019**, *1196*, 332–337. [\[CrossRef\]](#)
55. Rafaja, D.; Wüstefeld, C.; Dopita, M.; Motylenko, M.; Baetz, C. Capability of X-ray diffraction for the study of microstructure of metastable thin films. *IUCr* **2014**, *1*, 446–456. [\[CrossRef\]](#) [\[PubMed\]](#)
56. Cuscó, R.; Alarcón-Lladó, E.; Ibáñez, J.; Artús, L.; Jiménez, J.; Wang, B.; Callahan, M.J. Temperature dependence of Raman scattering in ZnO. *Phys. Rev. B Condens. Matter* **2007**, *75*, 165202. [\[CrossRef\]](#)
57. Kahouli, M.; Tounsi, N.; Mzabi, N.; Guermazi, H.; Guermazi, S. Enhanced structural and optical properties of ZnO nanopowder with tailored visible luminescence as a function of sodium hydroxide to zinc sulfate mass ratio. *Adv. Powder Technol.* **2018**, *29*, 325–332. [\[CrossRef\]](#)
58. Kanningini, G.A.; Azizi, S.; Nyoni, H.; Nixwel Mudau, F.; Mohale, K.C.; Maaza, M. Green synthesis and characterization of zinc oxide nanoparticles using bush tea (*Athrixia phylicoides* DC) natural extract: Assessment of the synthesis process. *F1000Research* **2022**, *10*, 1077. [\[CrossRef\]](#)
59. Al-Arjan, W.S. Zinc Oxide Nanoparticles and Their Application in Adsorption of Toxic Dye from Aqueous Solution. *Polymers* **2022**, *14*, 3086. [\[CrossRef\]](#)
60. Thommes, M.; Kaneko, K.; Neimark, A.; Olivier, J.; Rodriguez-Reinoso, F.; Rouquerol, J.; Sing, K. Physisorption of gases, with special reference to the evaluation of surface area and pore size distribution (IUPAC Technical Report). *Pure Appl. Chem.* **2015**, *87*, 1051–1069. [\[CrossRef\]](#)
61. Turcu, E.; Coromelci, C.G.; Harabagiu, V.; Ignat, M. Enhancing the Photocatalytic Activity of TiO<sub>2</sub> for the Degradation of Congo Red Dye by Adjusting the Ultrasonication Regime Applied in Its Synthesis Procedure. *Catalysts* **2023**, *13*, 345. [\[CrossRef\]](#)
62. Ghica, D.; Vlaicu, I.D.; Stefan, M.; Nistora, L.C.; Nistor, S.V. On the agent role of Mn<sup>2+</sup> in redirecting the synthesis of Zn(OH)<sub>2</sub> towards nano-ZnO with variable morphology. *RSC Adv.* **2016**, *6*, 106732–106741. [\[CrossRef\]](#)
63. Manabeng, M.; Mwankemwa, B.S.; Ocaya, R.O.; Motaung, T.E.; Malevu, T.D. A Review of the Impact of Zinc Oxide Nanostructure Morphology on Perovskite Solar Cell Performance. *Processes* **2022**, *10*, 1803. [\[CrossRef\]](#)
64. Fu, H.; Pan, C.; Yao, W.; Zhu, Y. Visible-Light-Induced Degradation of Rhodamine B by Nanosized Bi<sub>2</sub>WO<sub>6</sub>. *J. Phys. Chem. B* **2005**, *109*, 22432–22439. [\[CrossRef\]](#) [\[PubMed\]](#)
65. Hu, X.; Mohamood, T.; Ma, W.; Chen, C.; Zhao, J. Oxidative Decomposition of Rhodamine B Dye in the Presence of VO<sup>2+</sup> and/or Pt(IV) under Visible Light Irradiation: N-Deethylation, Chromophore Cleavage, and Mineralization. *J. Phys. Chem. B* **2006**, *110*, 26012–26018. [\[CrossRef\]](#) [\[PubMed\]](#)
66. Trenczek-Zajac, A.; Synowiec, M.; Zakrzewska, K.; Zazakowny, K.; Kowalski, K.; Dziedzic, A.; Radecka, M. Scavenger-Supported Photocatalytic Evidence of an Extended Type I Electronic Structure of the TiO<sub>2</sub>@Fe<sub>2</sub>O<sub>3</sub> Interface. *ACS Appl. Mater. Interfaces* **2022**, *14*, 38255–38269. [\[CrossRef\]](#) [\[PubMed\]](#)
67. Noman, M.T.; Amor, N.; Petru, M.; Mahmood, A.; Kejzlar, P. Photocatalytic behaviour of zinc oxide nanostructures on surface activation of polymeric fibres. *Polymers* **2021**, *13*, 1227. [\[CrossRef\]](#)
68. Nair, M.G.; Nirmala, M.; Rekha, K.; Anukaliani, A. Structural, optical, photo catalytic and antibacterial activity of ZnO and Co doped ZnO nanoparticles. *Mater. Lett.* **2011**, *65*, 1797–1800. [\[CrossRef\]](#)
69. Kaur, J.; Singhal, S. Facile synthesis of ZnO and transition metal doped ZnO nanoparticles for the photocatalytic degradation of Methyl Orange. *Ceram. Int.* **2014**, *40*, 7417–7424. [\[CrossRef\]](#)
70. Sultana, K.A.; Islam, M.D.T.; Silva, J.A.; Turley, R.S.; Hernandez-Viezcás, J.A.; Gardea-Torresdey, J.L.; Noveron, J.C. Sustainable synthesis of zinc oxide nanoparticles for photocatalytic degradation of organic pollutant and generation of hydroxyl radical. *J. Mol. Liq.* **2020**, *307*, 112931. [\[CrossRef\]](#)
71. Kiwaan, H.A.; Atwee, T.M.; Azab, E.A.; El-Bindary, A.A. Efficient photocatalytic degradation of Acid Red 57 using synthesized ZnO nanowires. *J. Chin. Chem. Soc.* **2018**, *66*, 89–98. [\[CrossRef\]](#)
72. Pingping, N.; Guanghui, W.; Pinghua, C.; Huitao, Z.; Qun, C.; Hualin, J. Optimization of Boron Doped TiO<sub>2</sub> as an Efficient Visible Light-Driven Photocatalyst for Organic Dye Degradation With High Reusability. *Front. Chem.* **2020**, *8*, 172. [\[CrossRef\]](#)
73. Tsoukleris, D.S.; Gatou, M.-A.; Lagopati, N.; Sygellou, L.; Christodouleas, D.C.; Falaras, P.; Pavlatou, E.A. Chemically Modified TiO<sub>2</sub> Photocatalysts as an Alternative Disinfection Approach for Municipal Wastewater Treatment Plant Effluents. *Water* **2023**, *15*, 2052. [\[CrossRef\]](#)

**Disclaimer/Publisher’s Note:** The statements, opinions and data contained in all publications are solely those of the individual author(s) and contributor(s) and not of MDPI and/or the editor(s). MDPI and/or the editor(s) disclaim responsibility for any injury to people or property resulting from any ideas, methods, instructions or products referred to in the content.